

# EIGER. II. First Spectroscopic Characterization of the Young Stars and Ionized Gas Associated with Strong H $\beta$ and [O iii] Line Emission in Galaxies at $z = 5-7$ with JWST

**Journal Article****Author(s):**

Matthee, Jorryt; Mackenzie, Ruari; Simcoe, Robert A.; Kashino, Daichi; Lilly, Simon J.; Bordoloi, Rongmon; Eilers, Anna-Christina

**Publication date:**

2023-06-10

**Permanent link:**

<https://doi.org/10.3929/ethz-b-000618850>

**Rights / license:**

[Creative Commons Attribution 4.0 International](#)

**Originally published in:**

The Astrophysical Journal 950(1), <https://doi.org/10.3847/1538-4357/acc846>



# EIGER. II. First Spectroscopic Characterization of the Young Stars and Ionized Gas Associated with Strong $H\beta$ and $[O III]$ Line Emission in Galaxies at $z = 5-7$ with JWST

Jorryt Matthee<sup>1</sup> , Ruari Mackenzie<sup>1</sup> , Robert A. Simcoe<sup>2</sup> , Daichi Kashino<sup>3,4</sup> , Simon J. Lilly<sup>1</sup> , Rongmon Bordoloi<sup>5</sup> , and Anna-Christina Eilers<sup>2</sup>

<sup>1</sup> Department of Physics, ETH Zürich, Wolfgang-Pauli-Strasse 27, Zürich, 8093, Switzerland; [mattheej@phys.ethz.ch](mailto:mattheej@phys.ethz.ch)

<sup>2</sup> MIT Kavli Institute for Astrophysics and Space Research, 77 Massachusetts Avenue, Cambridge, 02139, Massachusetts, USA

<sup>3</sup> Institute for Advanced Research, Nagoya University, Nagoya 464-8601, Japan

<sup>4</sup> Division of Particle and Astrophysical Science, Graduate School of Science, Nagoya University, Nagoya 464-8602, Japan

<sup>5</sup> Department of Physics, North Carolina State University, Raleigh, 27695, North Carolina, USA

Received 2022 November 15; revised 2023 March 13; accepted 2023 March 16; published 2023 June 12

## Abstract

We present emission-line measurements and physical interpretations for a sample of 117  $[O III]$  emitting galaxies at  $z = 5.33-6.93$ , using the first deep JWST/NIRCam wide-field slitless spectroscopic observations. Our 9.7 hr integration is centered upon the  $z = 6.3$  quasar J0100+2802—the first of six fields targeted by the EIGER survey—and covers  $\lambda = 3-4 \mu\text{m}$ . We detect 133  $[O III]$  doublets, but close pairs motivated by their small scale clustering excess. The galaxies are characterized by a UV luminosity  $M_{UV} \sim -19.6$  ( $-17.7$  to  $-22.3$ ), stellar mass  $\sim 10^8$  ( $10^{6.8-10.1}$ )  $M_{\odot}$ ,  $H\beta$  and  $[O III]_{4960+5008}$  EWs  $\approx 850 \text{ \AA}$  (up to  $3000 \text{ \AA}$ ), young ages, a highly excited interstellar medium, and low dust attenuations. These high EWs are very rare in the local universe, but we show they are ubiquitous at  $z \sim 6$  based on the measured number densities. The stacked spectrum reveals  $H\gamma$  and  $[O III]_{4364}$ , which shows that the galaxies are typically dust- and metal-poor ( $E(B-V) = 0.1$ ,  $12 + \log(O/H) = 7.4$ ) with a high electron temperature ( $2 \times 10^4 \text{ K}$ ) and a production efficiency of ionizing photons ( $\xi_{\text{ion}} = 10^{25.3} \text{ Hz erg}^{-1}$ ). We further show the existence of a strong mass–metallicity relation. The properties of the stars and gas in  $z \sim 6$  galaxies conspire to maximize the  $[O III]$  output from galaxies, yielding an  $[O III]$  luminosity density at  $z \approx 6$  that is significantly higher than that at  $z \approx 2$ . Thus,  $[O III]$  emission-line surveys with JWST prove a highly efficient method to trace the galaxy density in the Epoch of Reionization.

*Unified Astronomy Thesaurus concepts:* High-redshift galaxies (734); Galaxy formation (595); Reionization (1383); Interstellar medium (847); Chemical abundances (224)

*Supporting material:* figure set

## 1. Introduction

In the last two decades, extensive observations with the Hubble Space Telescope (HST) and ground-based telescopes have revealed the first glimpse of galaxies in the early universe at redshifts beyond the peak of cosmic star formation history ( $z \gtrsim 2$ ; Madau & Dickinson 2014). Most emphasis has been on mapping out the evolution of the number density distribution of Lyman-break galaxies (LBGs; e.g., Bunker et al. 2010; Finkelstein 2016; Bouwens et al. 2021). These galaxies are selected through a sharp color-drop in photometric data that is particularly strong at high redshift due to absorption from intervening neutral hydrogen (e.g., Madau 1995; Steidel et al. 1996). This is an effective technique that exploits the sensitive imaging capabilities on board the HST, but it is not very specific as samples contain interlopers, and the estimated redshifts are not very accurate (see Brinchmann et al. 2017 for a detailed comparison between spectroscopic and photometric redshifts at  $z \lesssim 6$ ).

Observations suggest that the cosmic star formation rate (SFR) density increased significantly by a factor  $\sim 10$  between  $z \sim 7$  and  $z \sim 2$ . The average properties of LBGs evolve significantly over this time-interval, with galaxies at higher redshifts being bluer and

smaller at fixed luminosity (e.g., Bouwens et al. 2014; Shibuya et al. 2015). A key feature is that galaxies in the early universe appear characterized by extremely strong nebular emission lines, in part due to their increasing specific star formation rates (sSFR; e.g., Stark et al. 2013; Mármol-Queraltó et al. 2016). The evidence for strong nebular  $H\beta + [O III]$  emission is the large color excesses in Spitzer/IRAC data covering the rest-frame optical (e.g., Zackrisson et al. 2008; Schaerer & de Barros 2009; Raiter et al. 2010; Labbé et al. 2013; Smit et al. 2014; Roberts-Borsani et al. 2016) and circumstantially the increasing fraction of strong Ly $\alpha$  emitters among LBGs with increasing redshift (e.g., Stark et al. 2011; Sobral et al. 2018; Kusakabe et al. 2020). However, the presence of these lines in large statistical samples of  $z \sim 6$  galaxies has not yet been confirmed spectroscopically.

Galaxies with extreme emission lines (EELGs; e.g., van der Wel et al. 2011) are present throughout the history of the universe (e.g., Izotov et al. 2018, 2021b). For example, Mrk 71 at a redshift of  $80 \text{ km s}^{-1}$  ( $z = 0.0003$ ) has a rest-frame  $[O III]_{4960,5008}$  equivalent width (EW<sub>0</sub>) of  $864 \text{ \AA}$  (Moustakas & Kennicutt 2006; Micheva et al. 2017). However, galaxies with such extreme EWs  $\approx 1000 \text{ \AA}$  are very rare in the low-redshift universe. At stellar masses  $\sim 10^8 M_{\odot}$ , the typical  $[O III]$  EW is  $20 \text{ \AA}$  in the Sloan Digital Sky Survey (SDSS; e.g., Alam et al. 2015), and only  $< 1\%$  of SDSS galaxies are an EELG. The typical EWs increase with redshift and are  $100-200 \text{ \AA}$  at  $z \sim 2$  (e.g., Khostovan et al. 2016; Malkan et al. 2017; Boyett et al. 2022), with a strong increase toward lower mass (Reddy et al. 2018b). Photometric inferences beyond  $z > 3$  suggest typical EWs of  $\approx 700 \text{ \AA}$  at  $z \sim 6-8$  with

similar mass dependencies (e.g., Labbé et al. 2013; De Barros et al. 2019; Endsley et al. 2021, 2022).

The physical conditions in the interstellar medium (ISM) that is associated to these young star-bursting systems are relatively unexplored at  $z > 3$ , in particular for low mass galaxies. Atacama Large Millimeter/submillimeter Array spectroscopy has revealed detections of strong  $88 \mu\text{m}$  [O III] line emission in a handful of galaxies at  $z \sim 7$  (e.g., Inoue et al. 2016; Hashimoto et al. 2019; Tamura et al. 2019; Witstok et al. 2022) showing high [O III]/[C II] line ratios suggestive of a high ionization parameter ( $\approx 5$ ; Harikane et al. 2020). The JWST is now set to transform this field by enabling sensitive rest-frame optical spectroscopy at  $z \approx 3\text{--}9$ . The first commissioning data have already revealed strong [O III] line emission at  $z = 4\text{--}9$  in a handful of objects (Sun et al. 2022a, 2022b; Rigby et al. 2023) and various other faint lines suggestive of very young ages, low metallicities, and a highly ionized ISM (e.g., Brinchmann 2022; Carnall et al. 2023; Curti et al. 2023; Katz et al. 2023; Rhoads et al. 2023; Schaerer et al. 2022; Tacchella et al. 2022; Taylor et al. 2022; Trump et al. 2023). Large surveys of statistical samples are soon anticipated (e.g., Bunker et al. 2020).

In this paper, we present the characterization of a sample of 117 spectroscopically confirmed [O III] doublets at  $z = 5.33\text{--}6.93$  from the first observations of our large JWST Emission-line galaxies and the Intergalactic Gas in the Epoch of Reionization (EIGER; program ID 1243, PI Lilly) survey. As explained and motivated in detail in our survey paper (Kashino et al. 2023, hereafter Paper I), EIGER uses wide-field slitless spectroscopy (WFSS) with NIRC*am* to obtain complete samples of  $\text{H}\alpha$  and [O III] emission-line galaxies at  $z = 3\text{--}7$  in the fields of six bright quasars, at  $z = 6\text{--}7$ . The main goal of EIGER is to study the end stages of cosmic reionization and the metal enriched envelopes of early galaxies through cross-correlations between galaxies and hydrogen and metal absorption lines.

The survey design, observing strategy, and the first cross-correlation between galaxies and the  $\text{Ly}\alpha$  forest at  $z \sim 6$  in the field of the ultra-luminous quasar J0100+2802 at  $z = 6.33$  (Wu et al. 2015; Wang et al. 2016) are presented in Paper I. Here we will briefly present the observations and data reduction in Section 2. In Section 3, we present the techniques to identify emission-line galaxies in the grism data; we motivate a method to merge closely separated clumps into systems and present the method to measure line fluxes and model the spectral energy distributions (SEDs) of our data. In Section 4, we show the first spectroscopic evidence for strong rest-frame optical line emission in a large sample of galaxies at  $z \sim 6$  and measure the [O III] luminosity function (LF). Then we present the physical conditions (ionizing photon production efficiency, dust attenuation, gas-phase metallicity) in our sample of [O III] emitters based on spectroscopic measurements in Section 5. Our results are discussed in Section 6, and we summarize our results and their interpretation in Section 7.

Throughout this work, we assume a flat  $\Lambda$ CDM cosmology with  $H_0 = 67.4 \text{ km s}^{-1} \text{ Mpc}^{-1}$ , and  $\Omega_M = 0.315$  (Planck Collaboration et al. 2020). Magnitudes are listed in the AB system.

## 2. Data

The details of the survey design and data reduction are presented in Paper I. Here we briefly summarize these and highlight the aspects that are most relevant for this paper.

### 2.1. Observations

We use a combination of infrared imaging and WFSS of the high-redshift quasar J0100+2802 taken with NIRC*am* (Rieke et al. 2023) on the JWST (program ID 1243, PI Lilly). The spectroscopic component consists of grism integrations in the F356W filter using GRISMR that disperses spectra in the horizontal direction. The imaging data consist of F115W and F200W (short-wave channel) observations taken contemporaneously with the spectroscopy, and direct and out-of-field imaging in the F356W filter that covers the spectroscopic field of view. As detailed in Paper I, we employ a four-pointing mosaic centered on the quasar. A central region of about  $40'' \times 40''$  is observed during all four visits, with several further regions that are covered by two or one visits. The total area with spectroscopic coverage is  $25.9 \text{ arcmin}^2$ , of which  $\approx 4.6 \text{ arcmin}^2$  is covered by both NIRC*am* modules (A) and (B) (with reversed dispersion direction). The observations were undertaken on four visits on 2022 August 22–24 with a position angle of the pointing of  $236^\circ$ . The total grism exposure times range from 8.8 to 35.0 ks, whereas the direct imaging time ranges from 1.6 to 6.3 ks, and the imaging in the short wavelengths ranges from 4.4 to 23.8 ks, with the F200W imaging receiving about 35% more exposure time than the F115W imaging.

### 2.2. Imaging Data Reduction and Photometry

As detailed in Paper I, the NIRC*am* imaging data are reduced based on a combination of the `jdust` pipeline v-1.8.2<sup>6,7</sup> and additional post-processing procedures. We perform the standard steps from `Detector1` and `Image2` and aligned the images to a common astrometric reference system aligned to Gaia (Gaia Collaboration et al. 2018). We perform additional subtraction of the sky level and stray-light features (“wisps”) and masked large residual cosmic-ray features (“snowballs,” e.g., Merlin et al. 2022). Using a deep source mask, we filter the  $1/f$  noise in our exposures; inspired by Schlawin et al. (2020), we subtract the median sky in quarter rows, then columns, and finally in the four amplifiers. `Image3` is used to combine the post-processed images onto a common grid with the resolution  $0.03''/\text{pixel}$ .

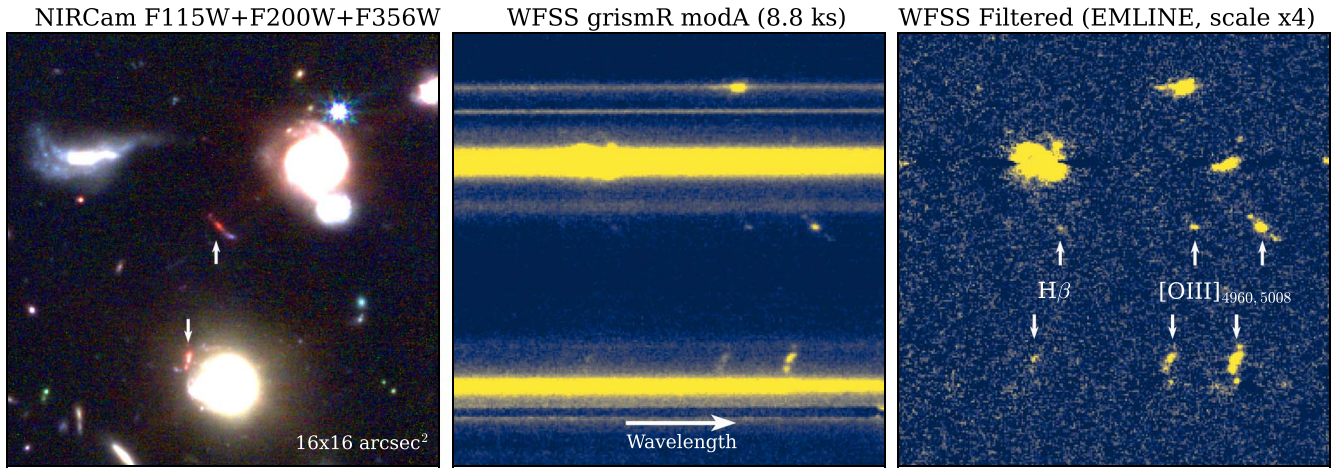
Aperture-matched photometry is performed using `SEXTRACTOR` (Bertin & Arnouts 1996) with the F356W imaging data as detection image. The higher-resolution F115W and F200W imaging data are convolved to match the point-spread function of the F356W imaging (see, Paper I). Magnitudes are measured with Kron apertures and the errors estimated from the random blank sky variation for apertures of different sizes, scaled to the local variance propagated by the pipeline (following Finkelstein et al. 2022). The typical  $5\sigma$  sensitivities are 27.8, 28.3, 28.1 in the F115W, F200W, and F356W imaging data, respectively, reaching to a magnitude deeper in the best regions (see Paper I).

### 2.3. WFSS Data Reduction

WFSS data are reduced with a combination of the `jdust` pipeline (version 1.7.0) and our `python` based processing

<sup>6</sup> <https://github.com/spacetelescope/jdust>

<sup>7</sup> We used the CRDS context `jdust_0988.pmap`, released on 2022 October 25 on the public server. This uses zero-points based on in-flight data (Boyer et al. 2022).



**Figure 1.** Demonstration of the JWST/NIRCam imaging and grism data and the continuum-filtering efficiency in a small  $16 \times 16$  arcsec<sup>2</sup> region that constitutes 0.3% of the data in the J0100+2802 field. The left panel shows a false-color composite of the F115W/F200W/F356W imaging and highlights the locations of two [O III] emitting systems identified in our data. These are particularly red due to the strong-line emission that falls in the F356W filter. The middle panel shows the dispersed grism image on the same subregion, while the right panel shows the result of our continuum-filtering methodology, which reveals various emission lines detected in the data.

steps as detailed in Paper I, which we summarize here. Each exposure is processed with `Detector1` step and assigned a WCS using `Spec2`. `Image2` is used for flat-fielding, and we additionally remove  $1/f$  noise and sky background variations by subtracting the median value in each column. The output after this step is named science image (*SCI*). Our main development is the separation of the *SCI* image in two components, *EMLINE* and *CONT*, which separate emission lines from the continuum. The continuum filtering subtracts the running median in the dispersion direction with a filter with a flexible kernel that has a hole in the center not to oversubtract the lines themselves. The process does not rely on the trace model or known positions of continuum sources, but does also not distinguish between continuum from sources themselves, or contamination. We illustrate the efficiency of the continuum-filtering methodology in Figure 1. Despite that one of the (multiple component) [O III] emitters is very close to a continuum bright galaxy, that spectral trace is not visible in the *EMLINE* image.

Spectral extraction for each object detected in the imaging (Section 2.2) is performed based on `grismconf`<sup>8</sup> using the latest (V4) trace models from N. Pirzkal, F. Sun, and E. Egami.<sup>9</sup> We have verified the accuracy of the trace model for GRISM in both modules in the F356W filter using extracted spectra of faint (F356W  $\sim 20$ ) stars in our data (see also Sun et al. 2022a) and apply pixel-level corrections when necessary. We extract 2D spectra from the *SCI*, *EMLINE*, *CONT*, and error (*ERR*) extensions in each of the (at max) 96 grism images. These are divided by the relevant sensitivity curve (hence correcting for different sensitivities in modules (A) and (B)), rectified for small curvature of the trace and scrunched to a common observed wavelength grid (from 3.0 to 4.0  $\mu\text{m}$  in steps of 9.75 Å). We then create stacked mean spectra, which were  $5\sigma$  clipped in three iterations. In addition, we create separate stacks for subsets of the individual visits and modules. We find that the spectra of sources observed in multiple visits (i.e., on different parts of the detector and/or on different modules) align excellently and have consistent fluxes.

<sup>8</sup> <https://github.com/npirzkal/GRISMCONF>

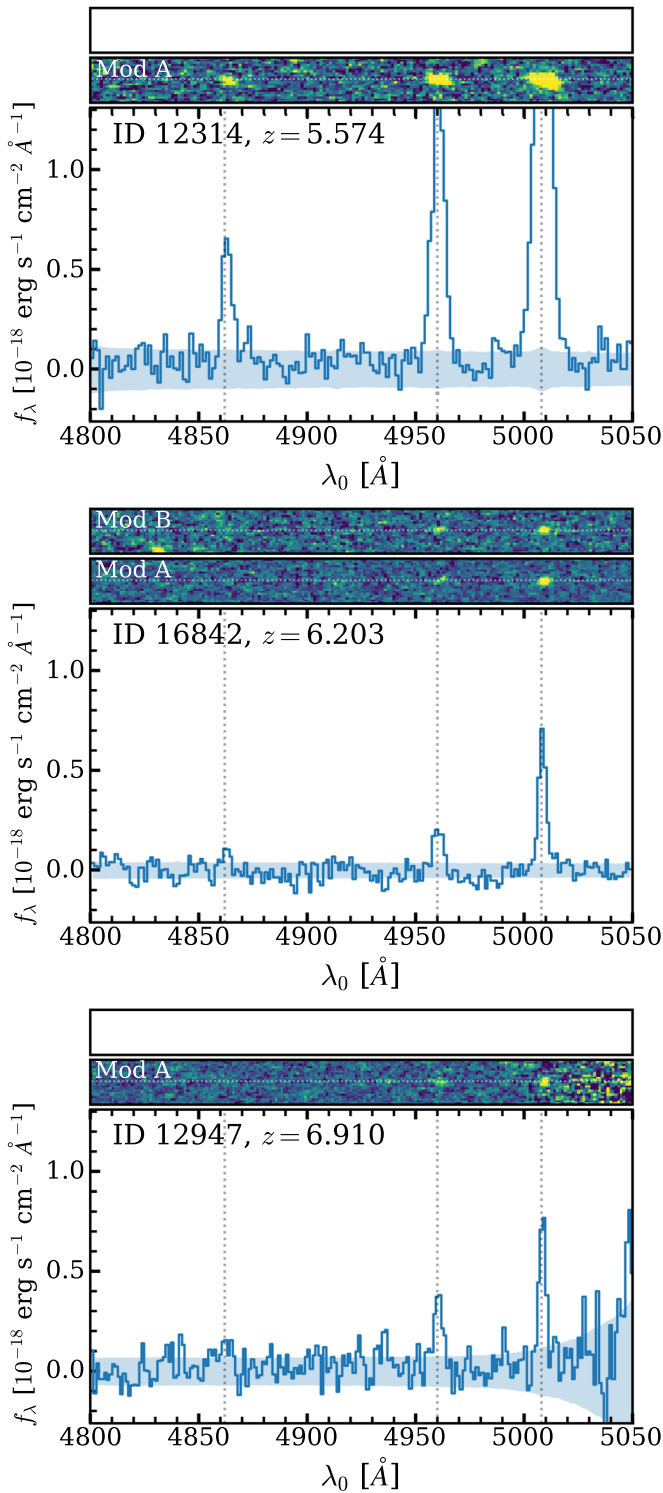
<sup>9</sup> [https://github.com/npirzkal/GRISM\\_NIRCAM](https://github.com/npirzkal/GRISM_NIRCAM)

### 3. Identification of [O III] Systems

#### 3.1. Detection Algorithms

As detailed in Paper I, we identify [O III] emitters with two complementary approaches, named the “backward” and the “forward” approach. In the backward approach, we identify emission-line pairs (such as [O III]<sub>4960,5008</sub>) or triplets (e.g., with H $\beta$ ) by running `SExtractor` directly on the combined continuum-filtered grism images that are stacked per visit and module, and then identify the corresponding galaxy on the direct image based on the observed wavelength that is estimated from the observed doublet separation. In the forward approach, we run `SExtractor` on the direct F356W image, and then extract a spectrum in the *EMLINE* image for each galaxy at its expected position based upon the tracing model, identifying galaxies for which candidate pairs of lines are detected close to the expected trace center. Lines are detected with a minimum signal-to-noise ratio (S/N) of 3. The  $3\sigma$  limiting sensitivity of the spectroscopic data varies across the field and with wavelength (by a factor  $\approx 2$ ), with the best sensitivity of  $0.6 \times 10^{-18}$  erg s<sup>-1</sup> cm<sup>-2</sup> at 3.8  $\mu\text{m}$ . In order to facilitate the line—galaxy association and the redshift identification of each of the lines, we limit ourselves to objects with at least two significant line detections.

In total, after careful visual inspections and reconciliation of the objects identified with the two methodologies and an iterative fine-tuning of the search parameters, we identify 133 resolved [O III] emitting components over  $z = 5.33\text{--}6.93$  with at least two detected emission lines with S/N > 3. Figure 2 shows three example spectra that are representative for the full sample. All H $\beta$ + [O III] spectra are shown in the online version of Figure 2. The typical S/N for the bright [O III]<sub>5008</sub> line is 14 (ranging from 6 to 70), and H $\beta$  is detected with S/N > 3 (5) in 68 (31) objects (detectable at  $z \gtrsim 5.5$  in our data). Only 3/133 objects were identified thanks to H $\beta$  (i.e., [O III]<sub>4960</sub> S/N < 3). We detect H $\gamma$  in two objects with S/N = 3.8 and 7.6, respectively. The catalog of [O III] emitters including their coordinates, confidence flags, and redshifts will be released with our survey Paper I.



**Figure 2.** Example emission-line 1D spectra of three representative [O III] emitters in our sample. Vertical dotted lines highlight the locations of  $\text{H}\beta$  and  $[\text{O III}]_{4960,5008}$ . Shaded regions show the noise level. The integrated S/N of  $\text{H}\beta$  ( $[\text{O III}]_{4960}$ ) in each panel are 13.8 (38.3), 4.5 (10.8), and 3.3 (7.4), respectively. (The complete figure set of 117 images is available.)

### 3.2. Definition of a System

While inspecting the [O III] emitters, we noticed that a significant number appear in closely separated pairs or multiples (see also Chen et al. 2023 for similar results based

on JWST imaging). Here, we argue for a simple definition of a *system* that can be easily mimicked in simulations.

Figure 3 shows false-color images of example [O III] emitters with multiple closely separated components. The object in the left panel is resolved in four components within  $0''.4$  ( $\sim 2$  kpc) while being at a close distance to a foreground galaxy suggesting possible galaxy–galaxy lensing (see also Figure 1). Several of such multiples exist in our sample, but such a close separation to the foreground galaxy is rare. The object in the middle panel shows two clumps with comparable luminosity and faint emission bridging these components. The right panel shows a group of five galaxies with a somewhat larger separation (maximally  $2''.5$  or  $\approx 15$  kpc). These five galaxies are identified as four clumps in our source catalog.

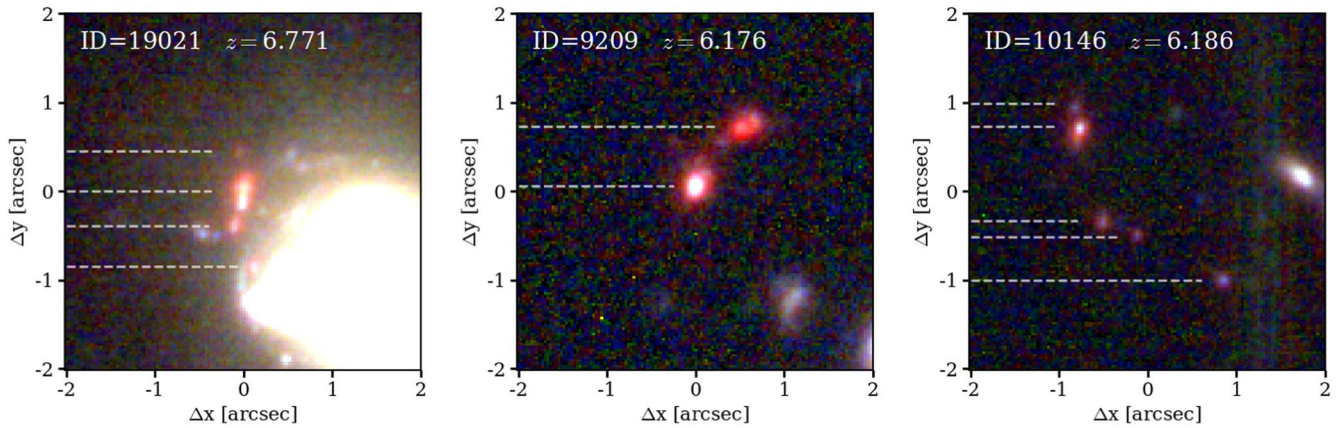
This simple compilation of galaxies in our data suggests that we should adopt a physical criterion to define an individual system, instead of relying on the specific choice of deblending parameters used by SExtractor, the orientation of the multiple components, or the specific spatial resolution of the data. Inspired by methodology in hydrodynamical galaxy formation simulations (e.g., Einasto et al. 1984; Springel et al. 2001), we merge components into groups using a friends-of-friends algorithm. Groups are identified by merging individual galaxies within a certain distance (linking length) to another object. We combine all the flux of the components within such a group and include it as a single object (*system*) in our analyses. The detailed investigation of the resolved properties of the clumps within these systems is deferred to a future paper with the full EIGER data.

The crucial parameter in the friends-of-friends algorithm is the linking length, which in our type of data should both be in the projected and redshift direction. We motivate the maximum linking length based on the projected autocorrelation function of the 133 [O III] emitting clumps shown in Figure 4. We measure the cumulative distribution of the number of object pairs as a function of their angular separation, normalized to the maximum number of pairs. The autocorrelation function of all [O III] emitters is compared to the autocorrelation function of the [O III] emitters with relative velocity differences less than  $1000 \text{ km s}^{-1}$  and to all objects in the parent catalog, which are close to randomly distributed. The [O III] emitters show a clear excess over the full catalog at separations  $< 2''$  (corresponding to  $\sim 12$  kpc at  $z \sim 6$ , which is close to the virial radius of halos with mass  $10^{11} M_\odot$  at  $z \sim 6$ ) indicative of amplified small scale clustering, for example due to satellites (e.g., Gelli et al. 2021). Interestingly, we find that all [O III] emitters that are within  $2''$  from each other are also within  $|\Delta v| < 1000 \text{ km s}^{-1}$  from each other and therefore plausibly physically associated.

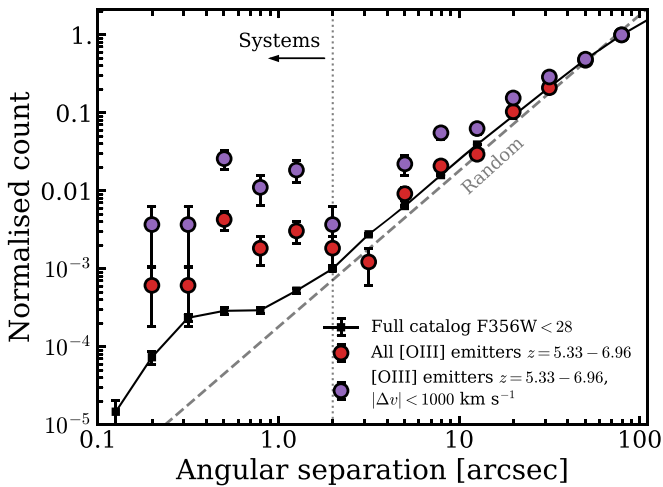
Motivated by these results, we match all [O III] emitters within a linking length of  $2''$  and merge the individually detected components within such groups together. As a result, 27 of the 133 [O III] emitters are merged to 13 groups, yielding a final sample of 117 [O III] emitting systems.

### 3.3. Flux Measurements

We measure total line fluxes of the galaxies from the grism EMLINE data using an optimal 1D extraction as follows. First, we collapse the profile of the  $[\text{O III}]_{5008}$  line over  $\pm 400 \text{ km s}^{-1}$  in the spectral direction ( $\pm 1000 \text{ km s}^{-1}$  for multiple component systems) and use the python package lmfit to fit the spatial profile with between 1 and 4 Gaussians based on visual inspection of the grism and imaging data and the relative



**Figure 3.** Example false-color F115W/F200W/F356W stamps of regions where we detect multiple [O III] emitting systems within  $2''$ , highlighting the diversity of these groups. The images are oriented with the position angle  $236^\circ$ . Each horizontal dashed line marks an [O III] emitting component that is resolved in the grism data.



**Figure 4.** The cumulative distribution of the number of object pairs as a function of their angular separation, normalized to the maximum number of pairs. The red symbols show the distribution of separations for all [O III] emitters, the purple symbols show the separations for pairs of [O III] emitters that have velocity differences less than  $1000 \text{ km s}^{-1}$ , and the black symbols for the full source catalog. Error bars represent poisson noise. The gray dashed line shows the expectation for a random distribution. The [O III] emitters show a significant excess in the number of pairs below a scale of  $2''$ , which corresponds to  $\approx 10 \text{ kpc}$ . All [O III] pairs within  $2''$  also happen to be closely separated in redshift ( $\Delta v = 600 \text{ km s}^{-1}$  at max).

goodness of fit. The vast majority of objects is small and unresolved and therefore fitted with a single Gaussian. We use the shape of the [O III] $_{5008}$  line as it is always the brightest line in the spectra of our galaxy sample. Measurements are independently performed for modules (A) and (B), and, in case both are available, we average them. Spatially resolved line ratios will be explored in a future paper.

Then, we extract the full 1D continuum-filtered (EMLINE) spectrum assuming this same spatial profile. Since we noticed that the uncertainties that are propagated by the pipeline significantly underestimate the noise level, we rescale the noise level of the 2D EMLINE spectrum by enforcing that the standard deviation of empty-sky pixels that cover wavelengths  $\lambda = 3.15\text{--}3.95 \mu\text{m}$  in our spectrum equals the mean noise level at the same wavelength range. Example 1D extracted spectra are shown in Figure 2.

Finally, we fit the spectral line profile of the [O III] $_{5008}$  line with between 1–3 Gaussians. The fitting is similarly performed

using a least-squares algorithm using `lmfit` and errors on the total line fluxes are propagated from the covariance matrix. The various components represent multiple closely separated clumps in the grism data, and we find no strong indication for separate dynamical components (e.g., broad wings) in the spectra of individual [O III] emitters. We then force the same spectral profile on the H $\beta$  and [O III] $_{4960}$  lines, conservatively allowing  $100 \text{ km s}^{-1}$  velocity offsets due to possible uncertainties in the wavelength solution, and measure their total line flux.

We find that the [O III] $_{4960}$ : [O III] $_{5008}$  ratio is consistent with the expected 1:2.98 within  $1\sigma$  for the vast majority of galaxies (100/117 total objects, where the line ratio is  $2.97 \pm 0.04$  on average). Uncertainties in the sensitivity curve at the edges of our wavelength coverage, weak contamination by foreground emission lines, or residuals from the continuum-filtering process leads to slightly different line ratios in the other 17 objects, with a slight skew toward lower ratios (with a ratio of  $1.98 \pm 0.18$  on average for these 17;  $2.87 \pm 0.07$  for the full sample).

### 3.4. SED Fitting

Our survey was designed to obtain a complete sample of spectroscopic redshifts and has less imaging coverage than typical extragalactic survey fields. For  $z \sim 6$  galaxies, we cover the rest-frame UV with two filters (F115W, F200W)<sup>10</sup> and have one rest-frame optical filter (F356W) that includes the lines covered by our WFSS. This challenges the characterization of the full SEDs of our galaxies.

On the other hand, our spectroscopic measurements of nebular line emission offer significant constraining power on the presence of young stellar populations (e.g., Leitherer et al. 1999; Matthee et al. 2022a). Besides the strong emission lines, the ionizing radiation from the young stellar populations also powers the strong nebular continuum emission that may contribute substantially to the spectrum (Reines et al. 2010; Byler et al. 2017; Topping et al. 2022). For our data, this is particularly relevant because the nebular free-free continuum can boost flux at  $\lambda_0 \sim 3000 \text{ \AA}$ , which translates to our F200W

<sup>10</sup> While there is partial coverage in several HST and ground-based imaging filters, we here only include JWST imaging data as this leads to the most uniform coverage across the field. At the redshifts considered in this paper, optical data mostly probe wavelengths below Ly $\alpha$  and therefore do not help constrain stellar SEDs.

photometry. For these reasons, we use a self-consistent inclusion of photoionization modeling while fitting SEDs (see also, Carnall et al. 2023; Tacchella et al. 2022) using the `Prospector` code (Johnson et al. 2021) with nebular treatment based on `Cloudy` version 13.03 (Ferland et al. 1998; see Byler et al. 2017 for details).

Our sample selection criteria do not a priori distinguish whether the main dominant source of ionization is star formation or active galactic nucleus (AGN) activity. Generally, it is challenging to unambiguously separate AGN from starburst activity in this context (e.g., Tang et al. 2022), because our grism data lacks spectral coverage of important lines as [O II] and  $H\alpha$ /[N II]. As all lines that we detected have a full width half maximum narrower than  $\leq 400 \text{ km s}^{-1}$ , and have low stellar masses, and because no bright source has a simple point-source morphology, we assume that all galaxies are powered by star formation.

Specifically, we use `Prospector` to fit the F115W, F200W, and F356W photometry and  $H\beta$  and [O III] $_{4960,5008}$  fluxes. We conservatively estimate the relative grism-to-imaging spectro-photometric calibration to be uncertain at the 5% level, and increase all errors accordingly. The free parameters in our modeling are the total formed stellar mass, its metallicity and star formation history, the dust attenuation, the gas-phase metallicity, and the ionization parameter. The redshift is fixed to the spectroscopic measurement, and we assume a Chabrier (2003) initial mass function and MIST isochrones (Dotter 2016; Choi et al. 2016). The star formation history follows a delayed- $\tau$  model, i.e.,  $\psi(t) = \psi_0 t e^{-t/\tau}$ . The combined nebular and stellar emission is attenuated through a simple dust screen following a Calzetti et al. (2000) law.

We generally use uniform and wide priors: the stellar mass can vary between  $10^{6-10.5} M_\odot$ , the stellar metallicity between  $[Z/H] = -2.0$  and  $+0.2$ , the dust optical depth  $\tau = 0-2$ , the age varies between 1 Myr and the age of the universe at the redshift of each source, and the star formation scale factor  $\tau_T$  can vary from 100 Myr to 20 Gyr. The gas-phase metallicity spans  $12+\log(O/H) = 6.7-9.2$ , and the ionization parameter  $U$  is fit in the range  $-3$  to  $+1$  in log scale. We allow for these very high values of the ionization parameter to maximize the flexibility of the fits. We finally add a nuisance parameter with values between 0 and 1 that scales the nebular emission relative to that produced by the stellar populations following the `Cloudy` modeling. This nuisance parameter adds flexibility to account for a nonzero escape of ionizing photons or photoelectric absorption from ionizing photons within HII regions (e.g., Tacchella et al. 2022). For slit-based spectra, this factor also accounts for the possibility of differential slit loss between continuum and line-emitting regions. Our WFSS observations are not affected by slit loss, and therefore provide a useful point of comparison to observations of galaxies at similar redshift made with JWST’s *NIRSpec* microshutter array.

Example SED fits are shown in Figures 5 and 6. We find that our fits yield SEDs that are characterized by relatively young ages,  $t_{\text{age}} = 110^{+230}_{-80}$  Myr, where the errors show the 16th–84th percentiles. The age distribution is typically very narrow ( $\tau_T = 10.1 \pm 0.5$  Gyr). Because  $t_{\text{age}}/\tau_T \ll 1$  in nearly all cases, the delayed-tau SFR history is well approximated as a single burst with linearly increasing  $\psi(t)$ . There is little dust attenuation;  $E(B - V) = 0.14$  on average. The UV luminosities of our galaxies range from  $M_{\text{UV}} -17.7$  to  $-22.3$  (typically  $M_{\text{UV}} = -19.6$ ), and the masses span 3 orders of magnitude

from  $\log_{10}(M_*/M_\odot) = 6.8-10.1$  with a median mass of  $2 \times 10^8 M_\odot$ . The nuisance parameter is typically  $0.89^{+0.05}_{-0.20}$ . The `Cloudy` models suggest that the gas metallicity and ionization parameter are  $12+\log(O/H) = 7.9$ , and  $\log(U) = -0.4$ , but these are both not tightly constrained (i.e., uncertain by almost an order of magnitude in individual objects). This is likely due to complicated dependence of the [O III]/ $H\beta$  line ratio on metallicity and ionization parameter. This is further discussed in Section 5.3. Additional emission-line measurements not covered by our grism data, such as [O II], are required to better constrain the ionization parameter.

## 4. Strength of Emission Lines in $z \sim 6$ Galaxies

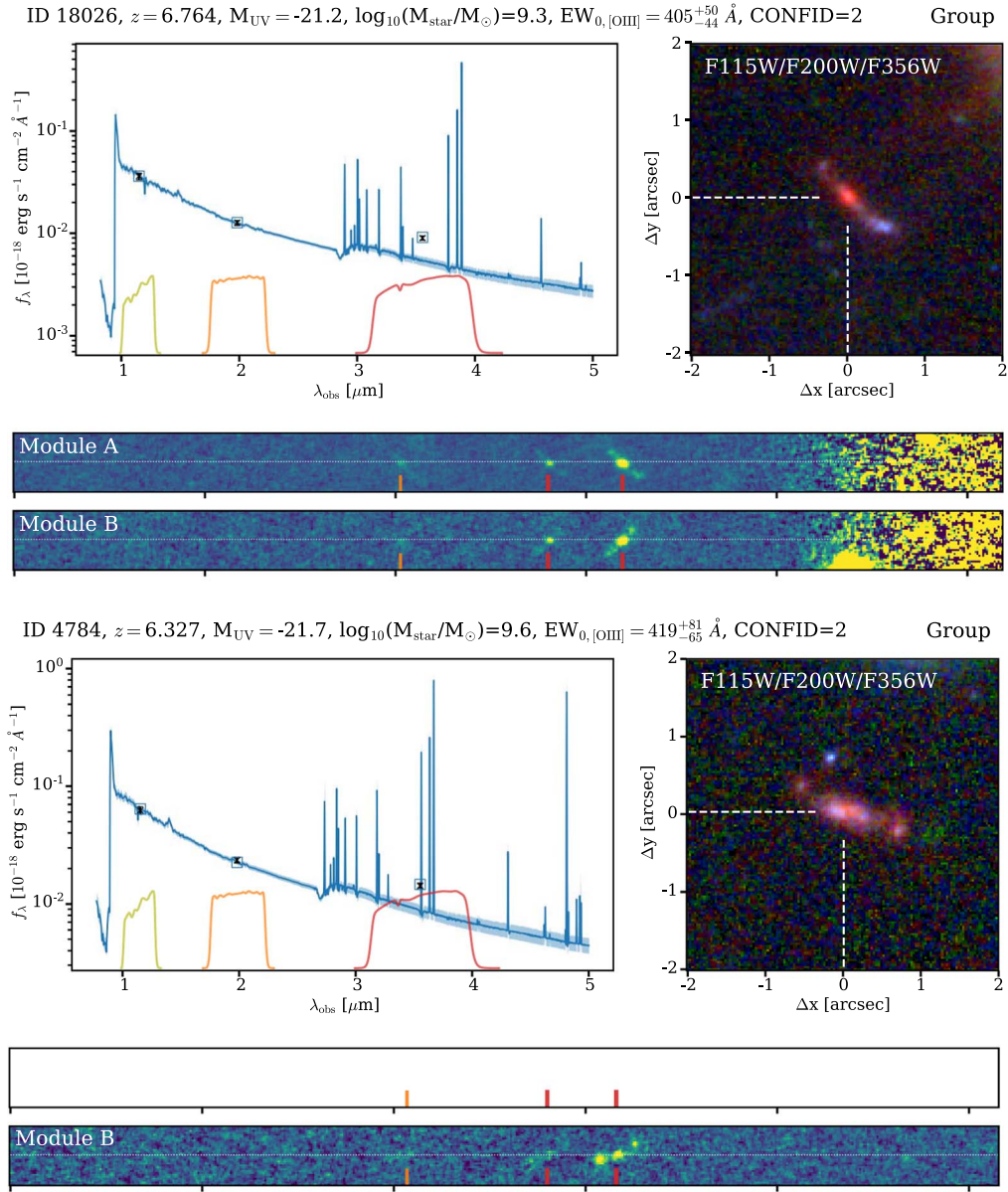
While the presence of strong emission lines was indicated in broadband photometry, high-redshift analogs (e.g., Izotov et al. 2021a), and the first JWST commissioning spectra (e.g., Sun et al. 2022b; Tacchella et al. 2022; Trump et al. 2023), our large spectroscopically confirmed sample finally allows us to investigate the presence of strong rest-frame optical emission lines in a broad sample of high-redshift galaxies. In this section, we first focus on the  $H\beta$  and [O III] EWs, we then present the correlation between UV and [O III] luminosity, and finally, we present our measurement of the [O III] luminosity function.

### 4.1. Optical Line EWs

#### 4.1.1. A Full Spectroscopic EW

Typically, SED modeling has been used to estimate the EWs of rest-frame optical lines in high-redshift galaxies (e.g., De Barros et al. 2019). However, in the absence of line-free photometry redward of the Balmer break, these EWs are uncertain. Hybrid methods, where line fluxes are measured from spectroscopy while photometry is used to constrain the continuum (Section 4.1.2), are further subject to uncertainties in the relative flux calibrations and aperture effects.

Preferably, the measurement of a line EW is based on spectroscopic data alone as this does not rely on the observatory’s (evolving) flux calibration model, but detecting the continuum is challenging when EWs are high. Grism spectroscopy contains significant continuum light from foreground galaxies, further complicating this measurement, as well as the measurement of the actual background. To overcome these limitations, we have visually inspected the WFSS data of all [O III] emitters and selected the 76 objects that are not strongly contaminated by foreground objects. We have verified that these 76 objects are representative of the full sample in terms of their UV and line luminosities (i.e., their  $L_{[\text{O III}]}-L_{\text{UV}}$  relation is similar to that of the total sample). We then extract 2D SCI spectra of these objects and create median stacks after masking the remaining foreground emission, shifting the spectra to the same rest-frame grid, and scaling them by their luminosity distance. A further small background subtraction is applied based on the median value in the off-center part of the stacked 2D spectrum. A median stack is preferred over a mean stack in order to further reduce the impact of unmasked contamination. We then perform an optimally weighted extraction by measuring the average spatial shape of the two [O III] lines. While we do not detect the continuum in the median stack of all these 76 objects ( $\text{EW}_0(H\beta+[O III]) > 970 \text{ \AA}$  at  $5\sigma$  significance), we do detect the continuum for the subset of 16 galaxies with UV luminosity brighter than  $M_{\text{UV}} < -20.5$ ; see Figure 7, with a signal to noise



**Figure 5.** Overview of the information that we can measure for two example [O III] emitters identified in the JWST data. For each object, we fit the spectral energy distribution using a composite stellar and nebular emission and dust attenuation model (see Section 3.4) to the three photometric data points and the  $H\beta$  and [O III] emission-line fluxes. Open squares show the modeled flux in the F115W, F200W, and F356W filters, respectively, while black squares show the measured photometry and its uncertainties. The main parameters that we derive from the SED models are the UV luminosity, the stellar mass, and the emission-line EWs. The false-color stamps reveal the diverse morphologies of the [O III] emitters whereas the generally red colors highlight the regions within the systems with strong-line emission. We display the 2D continuum-filtered spectra in both modules (A) and (B) (when available). The modules have opposite dispersion directions, where module (B) mirrors the image in the spatial direction. This is clearly illustrated in the spectrum of the object on top. Red and orange lines highlight the locations of  $H\beta$  and [O III], respectively. Both objects in this figure are identified as groups with three line-emitting components.

of 5.9. The  $H\beta$   $EW_0$  of this stack is  $116^{+26}_{-19} \text{ \AA}$ , and the  $[\text{O III}]_{4960+5008} EW_0 = 832^{+170}_{-122} \text{ \AA}$ . This confirms the extremely high average rest-frame optical emission lines in relatively UV bright galaxies at  $z \sim 6$  purely using spectroscopy.

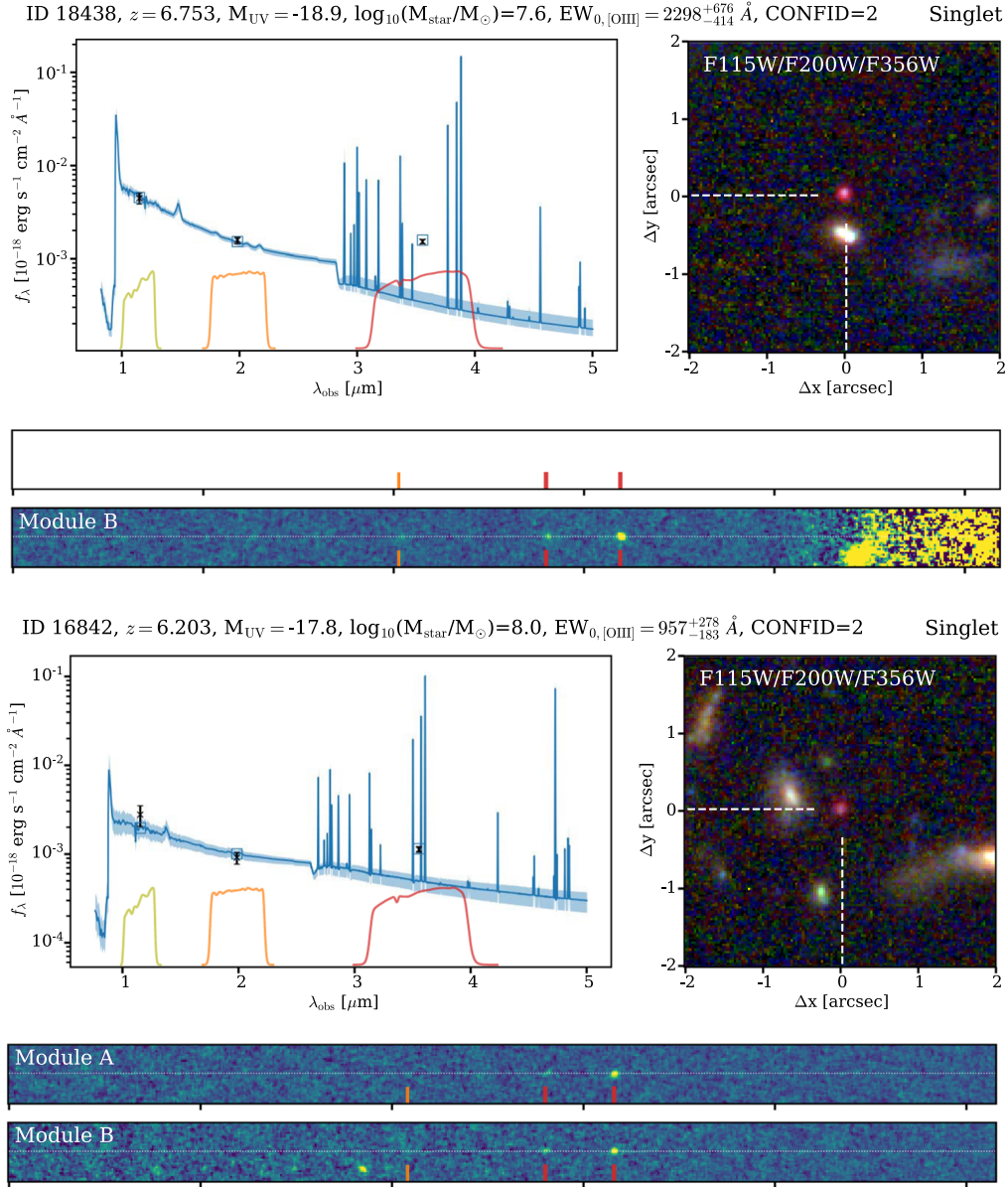
#### 4.1.2. Spectro-photometric EWs

With stacking we lose information on the distribution of EWs, and we were further not able to directly measure the EW in the majority of faint galaxies in our sample due to the nondetection of the continuum in the spectrum. We therefore explore EW measurements based on the imaging and WFSS

data combined. Line-flux measurements of the lines that contaminate the F356W photometry may directly inform us about the continuum level at these wavelengths and therefore the EW. However, there are uncertainties on the continuum slope within the filter and the contribution from faint undetected lines. We therefore primarily use physically motivated continuum levels based on the SED models (Section 3.4) to measure the EWs, but also compare these to more ad hoc measurements.

Our ad hoc measurement of the EW is done as follows: we model the flux measured in the F356W imaging data as a combination of continuum emission that follows a power law with slope  $\beta = -2$  and line emission from  $H\gamma$ ,  $H\beta$ , and [O III]





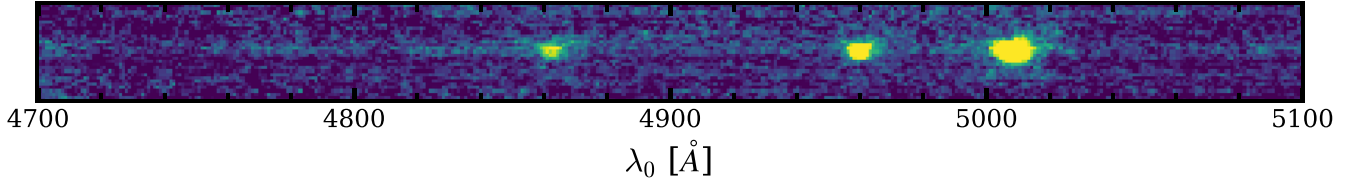
**Figure 6.** Same as Figure 5, but now highlighting isolated systems. These sources are representative for the fainter objects in our sample, which are typically small, compact systems with high EWs.

and fit this model to the photometry and line-flux measurements. We assume  $H\gamma/H\beta = 0.4$  based on our stacks (Section 5). The  $H\beta$  and  $[\text{O III}]$  EWs are derived from the model output. Our SED model-based EWs are derived from the posteriors of the SED fitting.

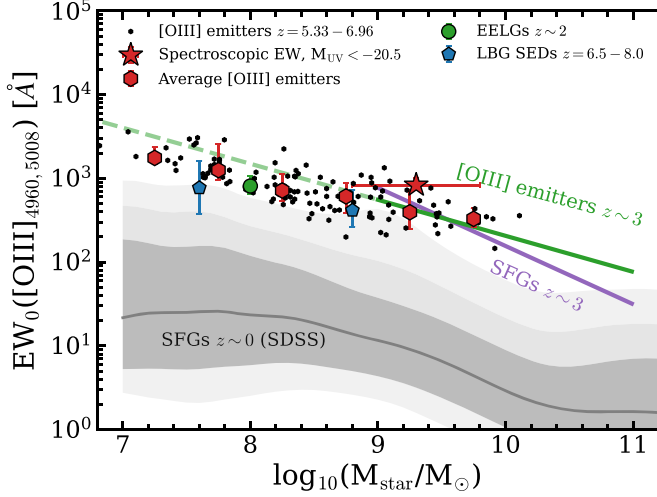
The median SED-based EW of our full sample is  $EW_0(H\beta + [\text{O III}]) = 850^{+750}_{-400} \text{ \AA}$ , which agrees very well with the ad hoc measurement of  $840^{+840}_{-440} \text{ \AA}$  (errors correspond to the 68% percentiles). The two measurements are typically consistent with a median ratio of 0.98 and a scatter of 0.2 dex. These EWs imply that  $40^{+22}_{-15}\%$  of the flux in the F356W photometry is due to line emission. For the bright subset of 16 galaxies with directly constrained EW, we find that the SED modeling yields  $EW_0(H\beta + [\text{O III}]) = 640^{+390}_{-340} \text{ \AA}$ , which is a factor  $\approx 0.7$  lower than the directly constrained  $EW_0(H\beta + [\text{O III}]) = 948^{+192}_{-138} \text{ \AA}$ , albeit within the uncertainties. This difference is both due to a lower modeled  $H\beta$  and  $[\text{O III}]$  EW.

In Figure 8, we show average EWs in subsets of mass and show broad agreement with the EWs at  $z = 6.5\text{--}8.0$  derived in recent SED fitting approaches including a continuum-free filter beyond the Balmer break (Endsley et al. 2022), and in low-redshift EELGs (van der Wel et al. 2011). The SED-derived EWs increase with decreasing mass and UV luminosity; see Figure 8. The mass dependence of the EW roughly follows the extrapolation of the trend observed at  $z \approx 3$  (Khostovan et al. 2016), i.e.,  $EW \propto \log_{10}(M_{\text{star}})^{-0.4}$ .

In general, Figure 8 shows that our measurements support the strong evolution toward extreme emission-line galaxies with EWs  $\gtrsim 1000 \text{ \AA}$  becoming *typical* at  $z \approx 6$  (this is further discussed in Section 6.1), while they only represent  $< 1\%$  of the galaxies in the SDSS. Our results are also in support of an increasing  $[\text{O III}]$  EW with decreasing mass, extending the dynamic range probed at  $z \approx 3$  by 2 orders of magnitude to masses  $\sim 10^7 M_{\odot}$  at  $z \approx 6$ .



**Figure 7.** The median stacked spectrum (without continuum filtering) of the 16 [O III] emitting galaxies at  $z = 6.28\text{--}6.81$  ( $z = 6.325$  on average) that are not contaminated by foreground objects and have a UV continuum brighter than  $M_{UV} < -20.5$ .  $H\beta$ , and the [O III] $_{4960,5008}$  lines are clearly seen. Continuum emission is detected with an S/N of 5.9, which allows direct spectroscopic measurement of the combined  $EW_0(H\beta + [O III]) = 948^{+192}_{-138}$  Å.

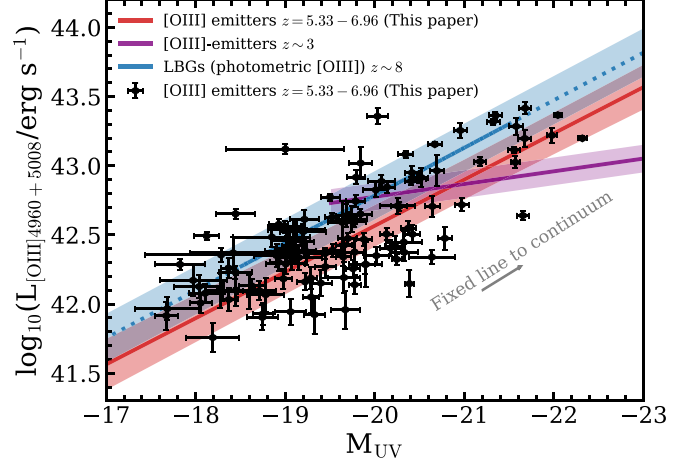


**Figure 8.** The relation between the [O III] EW and stellar mass at a wide range of redshifts. The spectroscopically determined EW is shown as a red star. We compare the average EWs in bins of mass (red hexagons; derived as detailed in Section 4.1.2 and error bars marking the 16th–84th percentiles) to extreme emission-line galaxies at  $z \approx 2$  (van der Wel et al. 2011) and UV-selected galaxies at  $z \approx 7$  (Endsley et al. 2022). We show the distribution of EWs in SDSS galaxies at fixed mass (corresponding to the  $1\sigma$ ,  $2\sigma$ ,  $3\sigma$  percentiles) in gray shades and also show the mass dependency of the EW in star-forming galaxies and [O III]-selected samples at  $z \approx 3$  (respectively Khostovan et al. 2016; Reddy et al. 2018a).

#### 4.2. $L_{[O III]}-L_{UV}$ Relation

Figure 9 compares the measured [O III] line luminosities with the UV luminosity of the galaxies we identified. Unexpectedly, both luminosities are strongly correlated, roughly following a slope with a fixed [O III] to UV luminosity ratio. For comparison, Figure 9 also shows the [O III]– $L_{UV}$  relation for relatively bright [O III] emitters at  $z \sim 3$  (Khostovan et al. 2016) and the inferred [O III] luminosities from SED fitting of UV-selected galaxies at  $z \sim 8$  (De Barros et al. 2019). Our results point toward a steeper relation compared to  $z \sim 3$ , with a significantly higher [O III] luminosity at fixed UV luminosity. We interpret this as a likely metallicity effect: at fixed UV luminosity, galaxies at  $z \approx 3$  plausibly have a higher metallicity, which acts to reduce the [O III] luminosity at a fixed SFR. The metallicity of our sample is further investigated in Section 5.3.

Our relation between UV and [O III] luminosity shows a comparable slope to the one measured at  $z \sim 8$  by De Barros et al. (2019), although our spectroscopic measurements are shifted to line luminosities that are 0.2 dex lower. Their derived  $EW(H\beta + [O III])$  of  $\approx 650$  Å is comparable to the typical EWs we measure in galaxies with similar UV luminosities ( $M_{UV} \approx -20$ ), suggesting that the differences are actually in the continuum level. Within our sample, the steep slope between [O III] and UV luminosity implies that there is not a lot of variation in the [O III] to optical continuum luminosities at  $z \sim 6$ . This could indicate little variation



**Figure 9.** The relation between the [O III] luminosity and UV luminosity for our sample of [O III] emitters (black data points), [O III] emitters at  $z \sim 3$  (purple shaded region; Khostovan et al. 2016) and the inferred [O III] luminosities in photometry of UV-selected galaxies at  $z \sim 8$  (blue shaded region; De Barros et al. 2019). The red line shows a simple linear fit to our data points  $\log_{10}(L_{[O III]_{4960+5008}}/\text{erg s}^{-1}) = 42.60 - 0.30(M_{UV} + 20)$  with a scatter of 0.27 dex.

in the [O III] EWs with UV luminosity, but because the UV-to-optical continuum ratio traces the Balmer break and experiences differences in nebular continuum emission, this trend needs to be interpreted with caution.

#### 4.3. [O III] Emission-line Luminosity Function

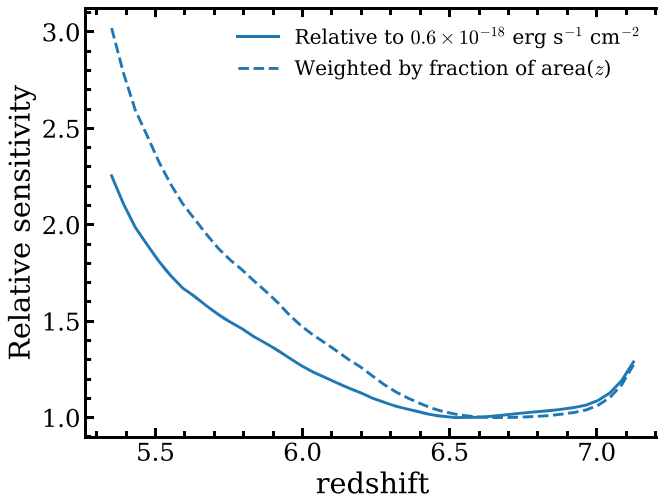
Here we derive the [O III] luminosity function at  $z \approx 6$  and compare it to lower redshifts (Khostovan et al. 2016), earlier estimates at  $z \sim 8$  (De Barros et al. 2019), and measured number densities (e.g., Sun et al. 2022b).

The luminosity function is measured using the classical  $1/V_{\text{max}}$  method (Schmidt 1968), where the number density in a given luminosity bin equals

$$\Phi(L) d \log L = \sum_i \frac{1}{c_i V_{\text{max},i}}, \quad (1)$$

where  $c_i$  is the completeness of source  $i$ , and  $V_{\text{max},i}$  is the maximum volume in which the source could have been detected. Since our selection criteria relies on the detection of both [O III] lines, our maximum volume is limited by the redshift range over which both the [O III] $_{4960,5008}$  lines can be detected ( $z = 5.33\text{--}6.96$ ). Likewise, an S/N = 3 detection of the fainter [O III] $_{4960}$  line is the limiting factor determining the completeness.

Our mosaic design yields significant spatial sensitivity variations due to large variations in exposure time and the large  $\approx 20\%$  difference in the sensitivity of the grism data in module (A) and module (B) (e.g., Rigby et al. 2023). Furthermore, both the sensitivity and the effective field of



**Figure 10.** The relative sensitivity of our grism data as a function of wavelength (here converted to the redshift of the [O III]<sub>4960</sub> line). The sensitivity is normalized to the maximum sensitivity of an S/N = 3 detection for a flux of  $0.6 \times 10^{-18} \text{ erg s}^{-1} \text{ cm}^{-2}$  at a redshift of  $z \approx 6.6$ . We illustrate the redshift dependency of the effective field of view of the grism data by weighting the sensitivity with the inverse of the maximum area at each redshift.

view depend on the wavelength of the line. These effects are illustrated in Figure 10, which shows the minimum flux of an S/N = 3 detection in our continuum-filtered data as a function of wavelength (here converted to redshift for [O III]<sub>4960</sub>), relative to the faintest flux detected at that significance ( $0.6 \times 10^{-18} \text{ erg s}^{-1} \text{ cm}^{-2}$ ). The sensitivity is optimal at  $z \approx 6.4$ – $6.9$  and a factor two lower at  $z \approx 5.5$ . Figure 10 also illustrates the impact of incomplete spectral coverage for a fraction of the field of view, which is increasingly important toward lower redshifts.

We model  $c_i$  and  $V_{\text{max},i}$  in our data self-consistently with our emission-line selection algorithm as follows. We measure  $V_{\text{max},i}$  by creating a 3D data cube of the  $3\sigma$  line-flux sensitivity as a function of wavelength and position. The cube contains cells of  $6''0 \times 4''5$ . In each cell, we combine all the emission-line line detections in the 2D spectra of the sources whose position is in each cell and measure the flux of the faintest line detected at S/N = 3, in steps of  $\Delta\lambda_{\text{obs}} = 20 \text{ nm}$ . In order to overcome shot-noise, we smooth the wavelength dependence of the limiting sensitivity with a uniform filter of 150 nm. To mitigate the higher shot-noise at the edges of our field of view (due to the lower sensitivity), we also smooth the spatial cells with a kernel that increases with the square of the distance to the center. This implies a maximum effective cell size of  $22'' \times 9''$  at the outer edges of our field of view. After creating this cube, we measure the fraction of the total volume for each [O III]<sub>4960</sub> line detection at R.A.<sub>*i*</sub>, decl.<sub>*i*</sub>, and  $\lambda_{\text{obs},i}$ . The completeness for each object,  $c_i$ , is determined by measuring the detection fraction of fake sources injected in the 2D spectrum at random positions within 250 Å and  $1''$  of the detection line itself. The flux of the fake sources is varied within the  $1\sigma$  confidence interval of the flux of each object. Sources are modeled as 2D Gaussians with an FWHM of  $0''13$ , which is representative for the detected lines.

The median completeness of our sample is 79% (ranging from 3% to 99.9%) with a primary dependence on line flux and secondary dependencies on observed wavelength and spatial location. Likewise, the fraction of the total survey volume in which a line can be detected depends mostly on observed wavelength, with a secondary dependence on flux. Typically,

**Table 1**  
The Field Number Densities of [O III] Emitters at  $z = 5.33$ – $6.96$  in the First EIGER Data in Units of  $\text{cMpc}^{-3} \text{ dlog}L^{-1}$  as a Function of [O III]<sub>5008</sub> Luminosity in Ergs per Second

$\log(L_{[\text{O III}]})$	$N$	$\langle c \rangle$	$\langle f \rangle$	$\log(\Phi_{\text{obs}})$	$\log(\Phi_{\text{corr}})$
$42.0 \pm 0.1$	12	0.38	0.72	−3.24	$-2.67^{+0.18}_{-0.20}$
$42.2 \pm 0.1$	18	0.45	0.82	−3.06	$-2.63^{+0.14}_{-0.16}$
$42.4 \pm 0.1$	19	0.74	0.85	−3.04	$-2.83^{+0.10}_{-0.12}$
$42.6 \pm 0.1$	10	0.84	0.84	−3.31	$-3.16^{+0.13}_{-0.17}$
$42.8 \pm 0.1$	8	0.95	0.90	−3.41	$-3.34^{+0.13}_{-0.19}$
$43.0 \pm 0.1$	8	0.95	0.89	−3.41	$-3.34^{+0.13}_{-0.19}$
$43.2 \pm 0.1$	4	0.95	0.92	−3.71	$-3.66^{+0.18}_{-0.30}$
$43.4 \pm 0.1$	2	0.91	0.84	−4.01	$-3.90^{+0.23}_{-0.53}$

**Note.** We mask the redshift range around the quasar J0100+2802.  $N$  is the number of objects in each bin,  $\langle c \rangle$  the average completeness,  $\langle f \rangle$  is the fraction of the area in which a line could be detected,  $\Phi_{\text{obs}}$  is the number density assuming the total volume and completeness, and  $\Phi_{\text{corr}}$  is the corrected number density taking the completeness and maximum volume into account. The errors combine the poisson noise with a 25% uncertainty on the completeness and volume correction added in quadrature. Logarithms are to base 10.

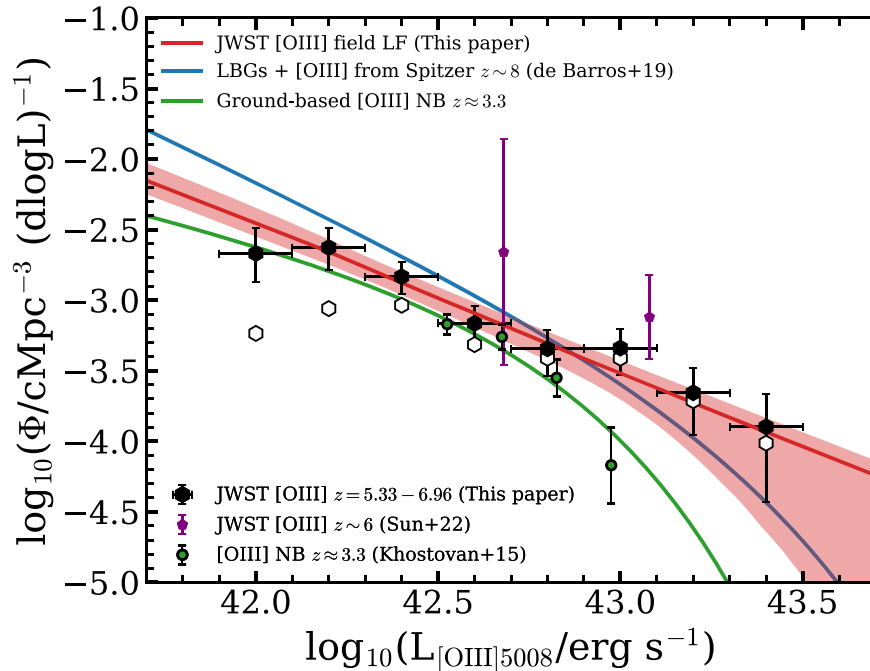
this fraction is 84% (ranging from 2% to 97%). The maximum volume of our survey spans  $25.9 \text{ arcmin}^2$  and  $z = 5.33$ – $6.96$ , which corresponds to  $1.06 \times 10^5 \text{ cMpc}^3$ .

As our survey targets a well-known luminous quasar at  $z = 6.33$ , our number densities of the total sample are likely not representative. Indeed, the quasar is embedded in a significant galaxy overdensity (which will be discussed in detail in R. Mackenzie et al. 2023, in preparation). To obtain an unbiased measurement of the luminosity function, we therefore mask the redshift range  $z = 6.30$ – $6.35$ , i.e.,  $\pm 1000 \text{ km s}^{-1}$  around the quasar and yield a maximum survey volume of  $1.03 \times 10^4 \text{ cMpc}^3$ . Further, in order not to depend on uncertainties in our completeness estimate, we only include the sources with a completeness of  $>10\%$  and remove the few objects identified thanks to H $\beta$  (where S/N [O III]<sub>4960</sub> < 3). This leaves 84 sources that were used to measure the [O III] luminosity function. We measure number densities in bins of 0.2 dex and report both the raw number of objects in each bin as well as the raw and corrected number densities in Table 1.

Typically, luminosity functions are parameterized with a Schechter (1976) function:

$$\Phi(L)dL = \Phi^* \left( \frac{L}{L^*} \right)^\alpha e^{-\frac{L}{L^*}} d\left( \frac{L}{L^*} \right), \quad (2)$$

where  $\Phi^*$  is the characteristic number density,  $L^*$  is the characteristic luminosity, and  $\alpha$  is the faint-end slope. As shown in Figure 11, our measured number densities of [O III] emitters at  $z \sim 6$  do not show significant evidence for an exponential decline at high luminosities. Therefore, fitting all three parameters of the LF (which we do in linear space) leads to significant uncertainties ( $\alpha = -0.24^{+1.24}_{-1.88}$ ,  $\log_{10}(\Phi^*) = -2.77^{+0.17}_{-5.27} \text{ cMpc}^{-3}$ , and  $\log_{10}(L^*/\text{erg s}^{-1}) = 42.18^{+3.49}_{-0.33}$ ). When we fit the LF while fixing the faint-end slope to  $\alpha = -2.0$ , which is the same as the UV LF at  $z \sim 6$  (e.g., Bouwens et al. 2021), we obtain the following constraints  $\log_{10}(\Phi^*) = -7.74^{+4.01}_{-0.15} \text{ cMpc}^{-3}$ , and  $\log_{10}(L^*/\text{erg s}^{-1}) = 46.94^{+0.05}_{-3.90}$ . While the fitted faint-end slope is uncertain, we note that a flatter faint-end slope compared to the UV LF may



**Figure 11.** The field [O III] luminosity function at  $z = 5.33\text{--}6.96$  (masking  $\pm 1000 \text{ km s}^{-1}$  around the redshift of the quasar; black hexagons). Open hexagons show the uncorrected number densities. The red line and shaded region show the fitted Schechter function, and the 68% confidence interval fixing the faint-end slope to  $\alpha = -2.0$ . Our number densities are compared to early JWST estimates at  $z \sim 6$  based on commissioning data (Sun et al. 2022b), narrow-band measurements at  $z \approx 3.3$  (Khostovan et al. 2015), and the inferred [O III] luminosity function at  $z \sim 8$  based on modeling the SEDs of UV-selected galaxies (De Barros et al. 2019).

not be unexpected in case the mass–metallicity relation (MZR) is steep, and lower mass galaxies emit increasingly less [O III] photons. This is further explored in Section 5.3.

When comparing our measured [O III] LF to results at lower redshifts (e.g.,  $z \approx 3$  Khostovan et al. 2015), we find remarkably little evolution in the [O III] LF over  $z = 3\text{--}6$ , in stark contrast to the decline of the UV LF and the cosmic SFR density over this epoch (e.g., Finkelstein 2016; Bouwens et al. 2021). Our number densities are lower than early JWST commissioning results (Sun et al. 2022b) and are comparable to those inferred by De Barros et al. (2019) based on SED modeling at  $z \approx 8$ , although with a clearly different shape. We discuss the interpretation of the [O III] luminosity function and the caveats further in Section 6.

## 5. The Physical Conditions in Early Galaxies

In addition to selecting and confirming the distances to galaxies, the measured emission lines also provide insights into the properties of galaxies. In this section, we first compare the variations in the  $H\beta$ -to-UV luminosity ratios and interpret this in the context of the production efficiency of ionizing photons. We then focus on line ratios, in particular [O III]/ $H\beta$ , which are interpreted in the context of the gas-phase metallicity. Here we limit ourselves to galaxies at  $z > 5.5$  where  $H\beta$  is spectrally covered.

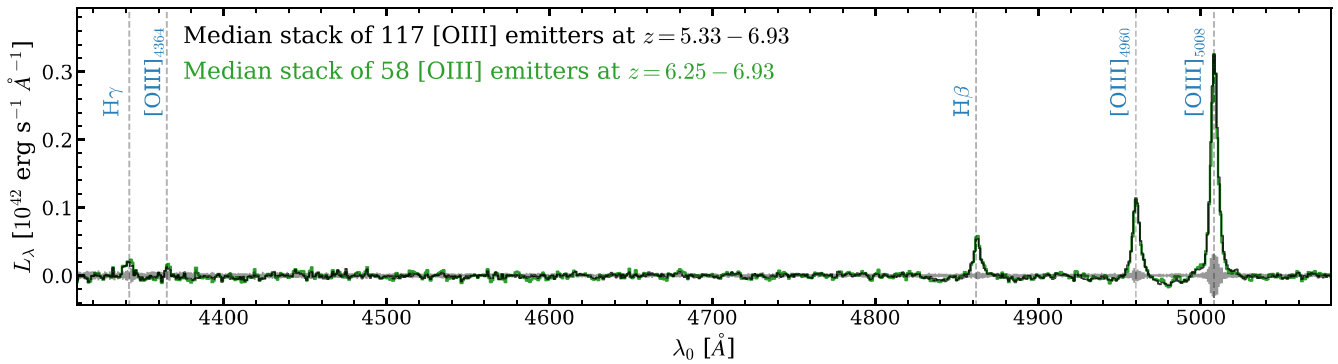
### 5.1. Stacking Methodology

While we base our results on detections of [O III] and  $H\beta$  in many individual galaxies, we also use the results from median stacks in various subsets of our galaxy sample as these stacked spectra allow the detection of fainter features. In Figure 12, we show the stacked 1D spectrum of the full sample of [O III] emitters. Since the rest-frame wavelength coverage bluewards of [O III] is

not uniform, one needs to interpret this stack with caution, but we show it for illustrative reasons here. The median stack is obtained after shifting the 1D spectrum of each [O III] emitter to the same rest-frame wavelength grid and rescaling it with the luminosity distance and redshift. We also account for slight residuals in the overall background and continuum subtraction by subtracting the median continuum level masking wavelengths of possible emission lines. The uncertainties are estimated by stacking 1000 bootstrap realizations of the sample. Figure 12 shows the strong  $H\beta$  and [O III] $_{4960,5008}$  emission lines, but also evidence for  $H\gamma$  and [O III] $_{4364}$ , which we will discuss below. We note that faint residuals of our continuum-filtering method are present around  $H\beta$  and [O III]. These are due to our emission-line mask missing some of the faint outskirts and/or companions of the emission-line detections while performing the continuum filtering. We also note that the line profiles of the stronger lines appear to have faint broad wings, but their interpretation is ambiguous as any spatial extent of the lines in the dispersion direction could mimic such dynamical features. We therefore only focus on line fluxes, which we measure using a two-component Gaussian model. By comparing the EMLINE and SCI stacks of the clean sample (see Section 4.1.1), we find that these residuals affect the flux of the [O III] $_{5008}$  line by 5%, and other lines by  $< 1\%$ . We therefore base the [O III] flux measurements of all our stacks on the measured [O III] $_{4960}$  flux and assume the intrinsic 1:2.98 ratio, verified in the stack of the clean sample. The measurements of the UV luminosity, median stellar mass, and  $H\beta$  and [O III] luminosities are listed in Table 2, where we also list various properties derived from these measurements.

### 5.2. The Production Efficiency of Ionizing Photons

Our SED fitting results indicate that our sample of [O III] emitters is characterized by relatively young stellar ages  $\sim 100 \text{ Myr}$  that power the strong emission lines. Here we interpret the emission-line strengths in the context of the



**Figure 12.** Median stacked 1D rest-frame emission-line spectrum of the full sample of 117 [O III] emitters at  $z = 5.33\text{--}6.93$  (black), and the subset of 58 galaxies at  $z = 6.25\text{--}6.93$  that has uniform coverage over the observed wavelength range shown here (green). The gray shaded region shows the uncertainty estimated through bootstrap resampling. Each spectrum is weighted equally. We highlight the wavelengths of  $H\gamma$ , [O III]<sub>4364</sub>,  $H\beta$ , and [O III]<sub>4960,5008</sub>, which are all detected at an integrated S/N > 5.

production efficiency of ionizing photons,  $\xi_{\text{ion}}$ , which is a crucial parameter in assessing the impact of galaxies on cosmic reionization (e.g., Robertson et al. 2013).  $\xi_{\text{ion}}$  can be measured from stellar population models (e.g., Duncan & Conzelmann 2015), but also using the Balmer recombination lines (e.g., Bouwens et al. 2016).

We detect the  $H\beta$  line in a significant fraction of the objects in the sample and can therefore estimate  $\xi_{\text{ion}} = \frac{L_{H\beta}}{c_{H\beta} L_{\text{UV}}}$ , where the line-emission coefficient  $c_{H\beta} = 4.86 \times 10^{-13} \text{ erg}$  for case (B) recombination with electron temperature  $10^4 \text{ K}$  and a zero escape fraction of ionizing photons (e.g., Schaerer 2003). Without applying dust corrections, we measure an average  $\log_{10}(\xi_{\text{ion}}/\text{Hz erg}^{-1}) = 25.5 \pm 0.1$ .

The dust correction is however critical in measuring  $\xi_{\text{ion}}$  accurately (Matthee et al. 2017; Shivaie et al. 2018). The stellar attenuation has been estimated for individual sources from the SED modeling and is typically low,  $E(B - V)_* = 0.11^{+0.09}_{-0.07}$ . Two objects have  $H\gamma$  detections that allow us to derive their nebular attenuation using the Balmer decrement and the observed  $H\gamma/H\beta$  ratio. Assuming an  $H\gamma/H\beta = 0.47$  in the unattenuated case, we measure  $E(B - V) = 0.30^{+0.13}_{-0.13}$  (Figure 13), and  $E(B - V) = 0.00^{+0.05}_{-0.00}$  for these two sources, respectively. These attenuations are similar to the stellar attenuations in the SED modeling and imply  $\log_{10}(\xi_{\text{ion}}/\text{Hz erg}^{-1}) = (25.39\text{--}25.55) \pm 0.20$  for these two sources in case the nebular and stellar attenuation following Cardelli et al. (1989), Reddy et al. (2016) attenuation curves, respectively.

In order to obtain a sample average, we estimate the typical nebular attenuation based on a stacked spectrum of the subset of 58 [O III] emitters at  $z = 6.25\text{--}6.93$  for which we have complete spectral coverage of  $H\gamma$ .  $H\gamma$  is detected with an S/N of 6.4 while the flux of  $H\beta$  is measured with an S/N of 17 (see Table 2). The observed  $H\gamma/H\beta$  ratio of  $0.41 \pm 0.06$  is, albeit uncertain, suggestive of little attenuation  $E(B - V)_{\text{gas}} = 0.14^{+0.16}_{-0.14}$ , consistent with the stellar attenuation. If we thus assume an attenuation of  $E(B - V) = 0.1$  for the total sample, we find a typical  $\log_{10}(\xi_{\text{ion}}/\text{Hz erg}^{-1}) = 25.31^{+0.29}_{-0.16}$ . We note that more precise measurements require better constraints on the attenuation.

This measurement of  $\xi_{\text{ion}}$  constitutes the first spectroscopic confirmation that the ionizing photon production efficiency in early galaxies appears higher than typical in galaxies at  $z \approx 0\text{--}2$  (e.g., Matthee et al. 2017; Atek et al. 2022); see Figure 14. Measurements of  $\xi_{\text{ion}}$  in rare high-redshift analogs such as

**Table 2**

Measurements of the Median Stack of Our Full Sample of [O III] Emitters from  $z = 5.33$  to 6.93 and the Subset at  $z > 6.25$  for which  $H\gamma$  and [O III]<sub>4364</sub> Are Measured

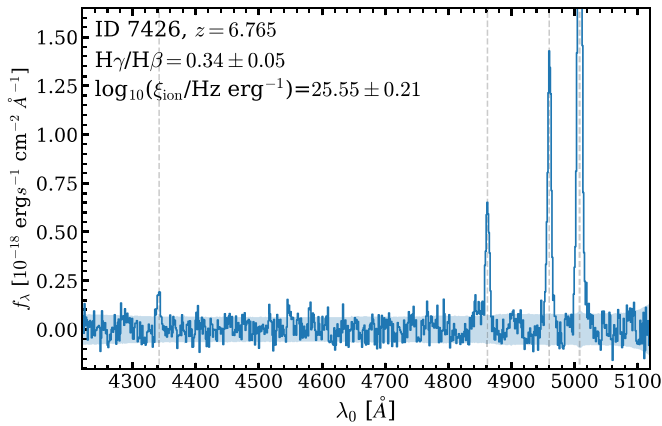
Property	Full Sample	$z > 6.25$
$N$	117	58
$M_{\text{UV}}$	$-19.6 \pm 0.1$	$-19.5 \pm 0.1$
$L(H\gamma)/10^{42} \text{ erg s}^{-1}$	...	$0.17 \pm 0.03$
$L([\text{O III}]_{4364})/10^{42} \text{ erg s}^{-1}$	...	$0.08 \pm 0.01$
$L(H\beta)/10^{42} \text{ erg s}^{-1}$	$0.38 \pm 0.02$	$0.41 \pm 0.02$
$L([\text{O III}]_{4960,5008})/10^{42} \text{ erg s}^{-1}$	$3.13 \pm 0.16$	$2.86 \pm 0.18$
$\log_{10}([\text{O III}]_{5008}/H\beta)$	$0.80 \pm 0.04$	$0.71 \pm 0.04$
$\log_{10}(M_*/M_{\odot})$	$8.38 \pm 0.07$	$8.45 \pm 0.09$
$\text{EW}_0(H\beta + [\text{O III}]_{4960,5008})/\text{\AA}$	$845 \pm 70$	$860 \pm 90$
$E(B - V)_{\text{gas}}$	...	$0.14^{+0.16}_{-0.14}$
$\text{SFR}(H\beta)/M_{\odot} \text{ yr}^{-1}$	$4 \pm 1$	$5^{+4}_{-2}$
$\log_{10}(\xi_{\text{ion}}/\text{Hz erg}^{-1})$	$25.3 \pm 0.2$	$25.31^{+0.29}_{-0.16}$
$T(O^{++})/10^4 \text{ K}$	...	$2.2 \pm 0.2$
$12 + \log_{10}(O/H)_{\text{O3H}\beta}$	$7.41 \pm 0.10$	$7.25 \pm 0.08$
$12 + \log_{10}(O/H)_{\text{direct}}^{\ddagger}$	...	$7.38 \pm 0.09$

**Note.** Line luminosities are not corrected for attenuation. For the full sample, the  $H\beta$  luminosity is dust-corrected assuming  $E(B - V) = 0.1$  based on the SED fits when measuring SFR and  $\xi_{\text{ion}}$ . As detailed in Section 5.2, we use an appropriate conversion between  $H\beta$  luminosity and SFR for the typical ionizing photon production efficiency.

<sup>a</sup> Based on assuming [O III]/[O II] =  $8 \pm 3$ .

green pea galaxies and Ly $\alpha$  emitters at  $z \approx 0\text{--}2$  with high [O III] EWs that are comparable to the lower mass galaxies in our sample (Table 3) show higher values of  $\xi_{\text{ion}}$  (Schaerer et al. 2016; Tang et al. 2019; Matthee et al. 2021), suggestive of significant variation among the galaxies. Our results are along the trend of increasing  $\xi_{\text{ion}}$  at fixed mass (Matthee et al. 2017) following the evolution of the  $H\alpha$  EW.

The ionizing photon production efficiency is also related to the measurement of SFR through the Balmer lines. In the standard SFR calibrations from Kennicutt & Evans (2012), equating the UV SFR to the  $H\alpha$  SFR implies  $\log_{10}(\xi_{\text{ion}}/\text{Hz erg}^{-1}) = 25.12$ . The higher measured  $\xi_{\text{ion}}$  implies that fewer stars are required to power the same  $H\alpha$  (or  $H\beta$ ) luminosity (e.g., Theios et al. 2019). Following the scaling in Table 2 from Theios et al. (2019), we assume an SFR- $L(H\alpha)$  conversion of  $\log_{10}(L(H\alpha) M_{\odot} \text{ yr}^{-1} \text{ erg}^{-1} \text{ s}^{-1}) = 41.59$  appropriate for our measured value of  $\xi_{\text{ion}}$ . Computing the  $H\alpha$  luminosity from the measured  $H\beta$  luminosity and assuming  $E(B - V) = 0.1$ , this implies a typical



**Figure 13.** 1D spectrum of one of the most luminous [O III] emitters in our sample, which shows detections of H $\gamma$  (integrated S/N = 7.6), H $\beta$ , and [O III]<sub>4960,5008</sub>. Note that the region of H $\gamma$  and [O III]<sub>4364</sub> is covered only for galaxies at  $z > 6.25$ .

$\text{SFR}(\text{H}\beta) = 4 \pm 1 M_{\odot} \text{ yr}^{-1}$  for the full sample. For the subset at  $z > 6.25$  where we directly constrain the nebular attenuation, we find a typical  $\text{SFR}(\text{H}\beta) = 5^{+4}_{-2} M_{\odot} \text{ yr}^{-1}$ .

### 5.3. Ionization Conditions and Gas-phase Metallicity

In Figure 15, we show the locations of our sample of [O III] emitters on the so-called “MEx” (mass–excitation) diagram (Juneau et al. 2011). Our sample of [O III] emitters has an average [O III]/H $\beta$  = 6.3, which is very high compared to typical galaxies in the SDSS with similar mass. We stress that a high [O III]/H $\beta$  ratio was not a strict selection requirement in our galaxy search, and this result thus reflects a physical property of this sample of galaxies. The average [O III]/H $\beta$  ratio in our sample is similar to the typical values measured in green pea galaxies at  $z \approx 0.3$  (e.g., Yang et al. 2017). We also show the measurements in the stacked spectra of four subsets of [O III] emitters split by stellar mass. Our measurements (listed in Table 3) extend the trend of an increasing [O III]/H $\beta$  with decreasing mass at high redshift (Sanders et al. 2020), although this trend flattens at masses below  $10^9 M_{\odot}$  and suggestively turns over below  $\lesssim 10^8 M_{\odot}$ . Our detection rate of galaxies with low [O III]/H $\beta$   $\lesssim 3$  ratios is highest at intermediate masses, which highlights significant scatter in these line ratios at fixed mass. We discuss these objects in Section 6.3.

The interpretation of the trend between [O III]/H $\beta$  and mass is not straightforward as the [O III]/H $\beta$  ratio is sensitive to variations in both the excitation state and the gas-phase metallicity. The relation between the gas-phase metallicity and [O III]/H $\beta$  is double-valued with a peak at  $12 + \log(\text{O}/\text{H}) \approx 7.7$ , and [O III]/H $\beta \approx 6$  (e.g., Bian et al. 2018; Curti et al. 2023; Nakajima et al. 2022). To illustrate this effect, the purple line in Figure 15 shows the expected relation between [O III]/H $\beta$  and mass assuming the Bian et al. (2018) strong-line calibration derived in local analogs of high-redshift galaxies, and the MZR at  $z \approx 6$  in the FIRE simulation (Ma et al. 2016),<sup>11</sup> which shows a similar behavior as observed in our stacks. This comparison implies that the metallicities of our [O III] emitters with mass  $\approx 10^{8-9} M_{\odot}$  are close to the metallicity where the relation between [O III]/H $\beta$  and metallicity peaks. We thus conclude

that the extremely high typical [O III] EWs in the majority of our sample are found in galaxies with ISM conditions that give rise to the maximum [O III] luminosity at given H $\beta$  luminosity (and thus, plausibly, at a given SFR).

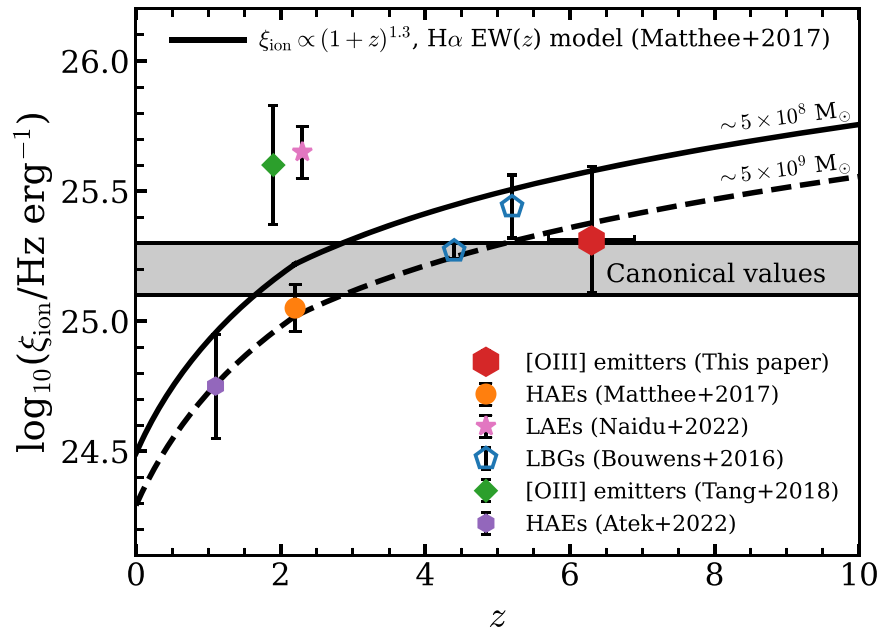
Surprisingly, we detect the temperature-sensitive [O III]<sub>4364</sub> line in the stacked spectrum of [O III] emitters at  $z > 6.25$  (where we have full coverage for this line and H $\gamma$ ); see Figure 16. After correcting the [O III]<sub>5008</sub>/[O III]<sub>4364</sub> ratio for dust attenuation using the measured Balmer decrement, we measure an electron temperature  $T(\text{O}^{++}) = 2.2 \pm 0.2 \times 10^4 \text{ K}$  using P<sub>Y</sub>Neb (Luridiana et al. 2015) assuming an electron density of  $300 \text{ cm}^{-3}$  (e.g., Sanders et al. 2016; Curti et al. 2023). While this is a fairly high electron temperature, it is not extreme compared to other recent measurements in high-redshift galaxies or extremely low metallicity galaxies in the nearby universe (e.g., Katz et al. 2023) and in line with early galaxies showing highly ionized and heated ISM.

The measurement of the electron temperature allows a direct estimate of the  $\text{O}^{++}$  abundance. Following the methodology outlined in Pilyugin et al. (2006) and propagating the uncertainties in the various line ratios, we measure  $12 + \log_{10}(\text{O}^{++})_{\text{direct}} = 7.21 \pm 0.08$ . We need to assume an [O III]/[O II] ratio to estimate the total gas-phase metallicity as our spectra do not cover the [O II]<sub>3727,3729</sub> line. Based on empirical scalings of the [O III]/[O II] ratio with line EW and electron temperature (e.g., Reddy et al. 2018b; Katz et al. 2023), we assume [O III]/[O II] =  $8 \pm 3$ . We then find a slightly higher total gas-phase metallicity of  $12 + \log_{10}(\text{O}/\text{H})_{\text{direct}} = 7.38 \pm 0.09$ . This estimate is within  $1\sigma$  agreement with the estimate based on [O III]/H $\beta$  using the strong-line calibration from Bian et al. (2018) assuming it is on the lower metallicity branch, which results in  $12 + \log_{10}(\text{O}/\text{H})_{\text{O3H}\beta} = 7.25 \pm 0.08$ .

Now, under the assumption that the Bian et al. (2018) calibration is also applicable for our stacks in subsets of mass, we estimate gas-phase metallicities for these subsets and list them in Table 3. Based on the relation between [O III]/H $\beta$  and mass that is shown in Figure 15, we assume that our two most massive subsets are on the higher metallicity branch of the [O III]/H $\beta$ –metallicity relation, while the other subsets are on the lower branch. In Figure 17, we compare the  $T_e$ -based metallicity measurement of our median stack and our strong-line method based measurements in subsets of mass to recent measurements in early JWST spectra (e.g., Curti et al. 2023) and (rescaled) expectations from hydrodynamical simulations (Ma et al. 2016). Our strong-line method estimates are suggestive of a strong correlation between metallicity and mass, in line with expectations from the simulations. Our results extend the redshift evolution of a decreasing metallicity at fixed mass established from  $z \approx 0$  to 3 (e.g., Sanders et al. 2021), and our measurement for the sample averaged metallicity (from the  $T_e$ -method) is in line with the redshift evolution expected from these simulations.

We however note that the applicability of the specific strong-line calibration is uncertain. For example, our direct-method-based metallicity for the full stack of galaxies at  $z > 6.25$  is significantly lower than the strong-line-based metallicity of subsets with similar mass, where the mass is similar to the median mass of the full sample. While this could be due to calibration uncertainties, we remark that the line ratios measured in median stacks of samples with a relatively wide variation in line ratios—especially with values around the peak of a double-valued relation—may be challenging to interpret. Further, if we would use the Nakajima

<sup>6</sup> Similar to, e.g., Curti et al. (2023), we rescaled the FIRE MZR to match the absolute normalization of the measured MZR at  $z \approx 3$  by Sanders et al. (2021), but apply the redshift evolution measured in the simulation (Ma et al. 2016).



**Figure 14.** The ionizing photon production efficiency  $\xi_{\text{ion}}$  of various galaxy populations through cosmic times. Spectroscopic measurements are shown as filled symbols, while photometric inferences (e.g., Bouwens et al. 2016) are shown as open symbols. The average value of  $\xi_{\text{ion}}$  measured in our sample of [O III] emitters is somewhat higher than the canonical value (e.g., Robertson et al. 2013) and normal galaxies at low redshift (Matthee et al. 2017; Atek et al. 2022), comparable to LBGs at  $z \approx 5$ , and somewhat lower than  $\xi_{\text{ion}}$  measured in extreme emission-line galaxies at  $z \approx 2$  (Tang et al. 2019; Naidu et al. 2022).

**Table 3**

The Combined Rest-frame  $\text{EW}(\text{H}\beta + [\text{O III}]_{4960,5008})$  and  $[\text{O III}]_{5008}/\text{H}\beta$  Line Ratios in Stacks of Four Subsets of Our Sample (with  $\text{H}\beta$  Coverage at  $z > 5.5$ ) Split by Stellar Mass

$\log(M_*/M_\odot)$	$\text{EW}_{0,\text{H}\beta+[\text{O III}]} \text{ \AA}^{-1}$	$[\text{O III}]/\text{H}\beta$	$12 + \log(\text{O}/\text{H})$
7.5	$1870_{-590}^{+1200}$	$5.3_{-0.8}^{+0.9}$	$7.29_{-0.14}^{+0.15}$
8.2	$980_{-240}^{+670}$	$6.7_{-0.6}^{+0.6}$	$7.77_{-0.20}^{+0.22}$
8.9	$690_{-300}^{+340}$	$6.3_{-0.7}^{+0.9}$	$8.05_{-0.35}^{+0.12}$
9.5	$410_{-100}^{+200}$	$5.4_{-0.4}^{+0.5}$	$8.19_{-0.06}^{+0.06}$

**Note.** Uncertainties for the EW are the 16th–84th percentiles of the distribution of EWs within each subset, while uncertainties on line ratios are measurement errors. We convert these line ratios to a gas-phase metallicity based on the strong-line calibration by Bian et al. (2018); see text. Logarithms are to base 10.

et al. (2022) calibration for sources with high EWs, we find that the metallicities of our two lowest mass stacks would increase by  $\approx 0.2$  dex yielding milder redshift evolution at  $z \gtrsim 3$  and a shallower slope. Future follow-up targeting fainter lines such as  $[\text{O III}]_{4363}$  and ongoing efforts to recalibrate strong-line methods at high redshift will be able to relieve some of these caveats. Further, larger samples from the full EIGER data will enable stacks in subsets with smaller dynamic range.

## 6. Discussion and Outlook

Here we will discuss our results and provide an outlook of some results that can be anticipated with the observations of the full EIGER sample in six quasar fields.

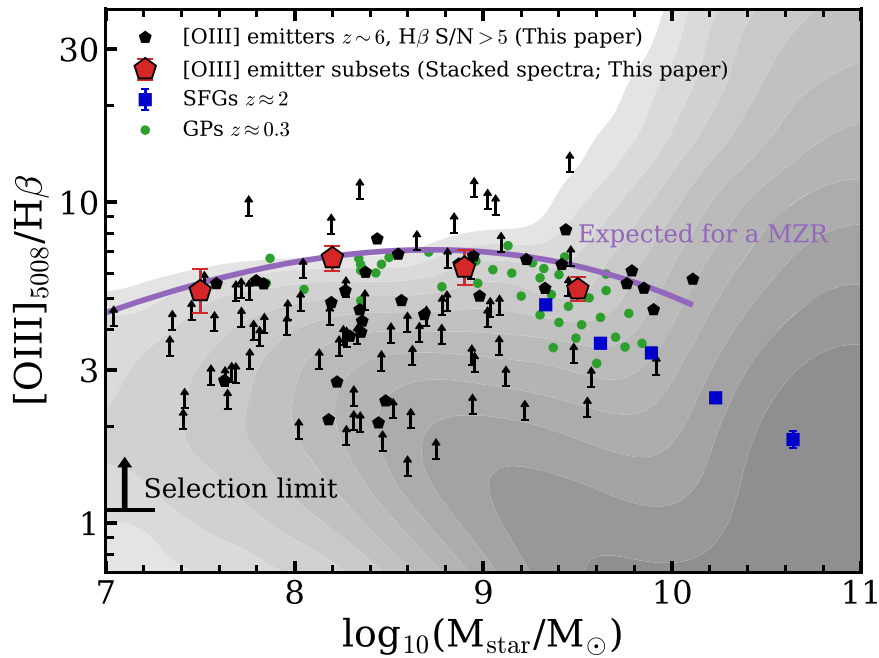
### 6.1. Strong [O III] Lines in Typical $z \sim 6$ Galaxies

Our large spectroscopic sample of [O III] emitting galaxies at  $z = 5.33\text{--}6.93$  confirms that strong rest-frame optical emission lines are abundant in distant galaxies, with typical EWs of

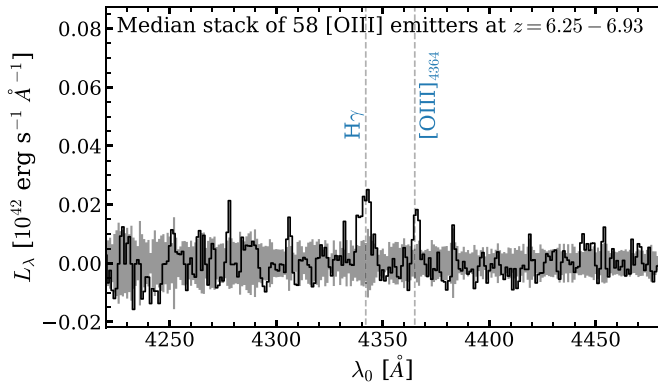
$\approx 850 \text{ \AA}$ , at UV luminosities  $M_{\text{UV}} \approx -19.5$  (Section 4.1). However, given that our sample is a line-selected sample, this result may not be surprising.

Our measured EWs are in broad agreement with inferences for UV-selected galaxies from SED modeling of the rest-optical light captured in Spitzer/IRAC or JWST filters (e.g., Smit et al. 2014; Roberts-Borsani et al. 2016; Endsley et al. 2021, 2022); see Figure 8. Furthermore, as shown in Figure 9, the relation between the [O III] line luminosity and the UV luminosity in our sample is only slightly lower compared to the inferred relation in UV-selected galaxies at  $z \sim 8$  (De Barros et al. 2019). These comparisons imply that these strong lines are typical in UV-selected galaxies and that there are no significant differences between samples that are selected either through the Lyman break or [O III] line emission.

We derive the UV luminosity function of our sample of [O III] emitters following the methods outlined in Section 4.3. As shown in Figure 18, we find that the number densities of [O III] emitters agree relatively well with the UV LF of LBGs measured by Bouwens et al. (2021) at  $z \sim 6$ , at least at luminosities in the range  $M_{\text{UV}} = -19.5\text{--}M_{\text{UV}} = -21.0$ . Similar to our [O III] LF, we have masked the redshift around the targeted quasar in order not to be biased by its overdensity. The resemblance of these number densities, despite that our target selection is completely different from the standard LBG selections (e.g., Bouwens et al. 2021), further demonstrates that the strong [O III] emission lines are typical in LBGs. At fainter UV luminosities, the number densities of [O III] emitters are significantly lower than the those of UV LF. This can be understood in the context of the [O III] EW distribution: for these faint galaxies, our emission-line survey only picks up galaxies with the most extreme EWs, which are no longer representative for the full sample at those UV luminosities. At the bright end, we note that cosmic variance may be particularly important. Three of the four galaxies with  $M_{\text{UV}} \lesssim -22$  are part of a large overdensity at  $z \approx 6.77$  Paper I. The addition of the five extra quasar fields from the EIGER



**Figure 15.** The location of our sample of [O III] emitters (black hexagons for  $H\beta$  detections with  $S/N > 5$ , arrows otherwise) on the mass–excitation diagram compared to galaxies in the SDSS (gray shades), green pea galaxies at  $z \approx 0.3$  (Yang et al. 2017), and star-forming galaxies at  $z \approx 2$  (Sanders et al. 2020). Red pentagons show the line ratios in stacks of subsets in mass. Most objects in our sample have a very high [O III]/ $H\beta$  extending the anticorrelation between [O III]/ $H\beta$  and mass identified at  $z \approx 2$  and comparable to the line ratios measured in green pea galaxies. The objects with the lowest [O III]/ $H\beta$  values are typically found among the intermediate masses in our sample. The purple line shows the expected relation assuming the Bian et al. (2018) strong-line calibration and the  $z \approx 6$  mass–metallicity relation (MZR) from the FIRE simulation (Ma et al. 2016).



**Figure 16.** Median stacked 1D spectrum of the subset of [O III] emitters at  $z = 6.25\text{--}6.93$  for which we have complete coverage of  $H\gamma$  and all redder lines, zoomed in on  $H\gamma$  and [O III] $_{4364}$ . The faint detections are at  $S/N$  of 6.5 and 5.3, respectively, but they allow us to constrain the typical dust attenuation and electron temperature.

program will be particularly useful to constrain the shape of the bright end of the LF.

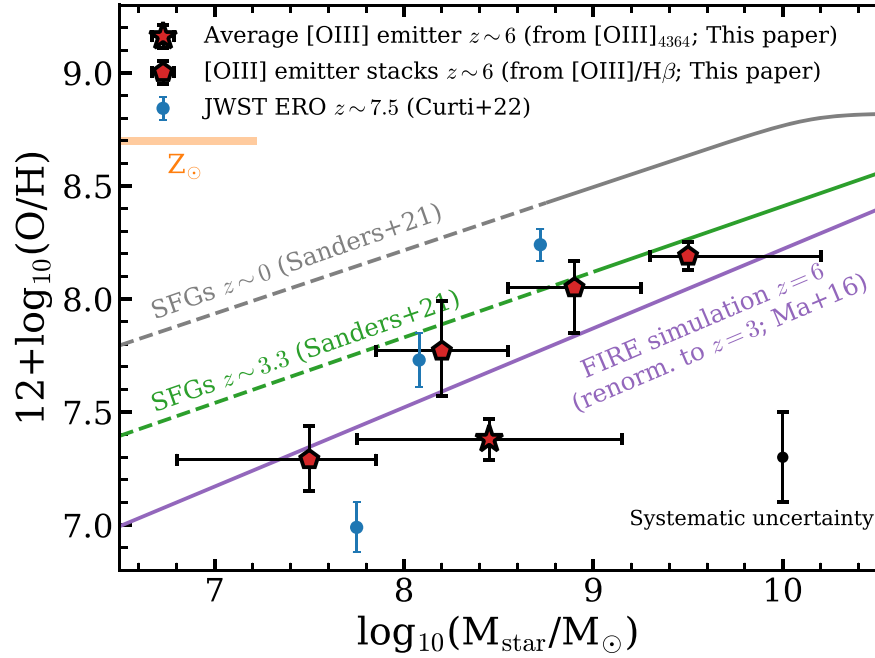
Based on our spectroscopically measured [O III] luminosity function and earlier measurements based on photometry or HST grism spectroscopy at lower redshifts, we now compare the evolution of the [O III] luminosity density  $\rho_{[\text{O III}]}$  to the evolution of the cosmic SFR density from Madau & Dickinson (2014) in Figure 19. The [O III] luminosity density evolves rather differently from the SFR density, with a significantly earlier peak in cosmic time. Whether the  $\rho_{[\text{O III}]}$  indeed peaks at  $z \approx 6$  as our results suggest, or perhaps between  $z \approx 4$  and 6, needs to be verified with future JWST observations at lower redshifts.

Despite an order of magnitude decline in the cosmic SFR density from  $z = 2$  to 6, we find that  $\rho_{[\text{O III}]}$  in fact increases from  $z = 2$ , to  $z = 6$  by a factor 2–5. Our explanation for this trend is a

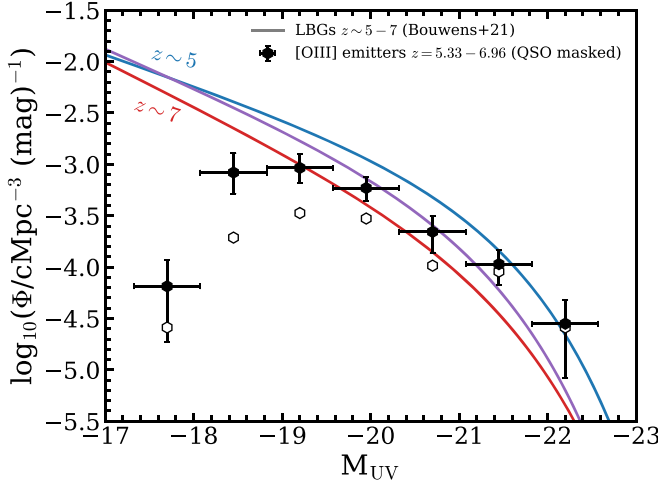
conspiracy between the evolving SFR density, the mass function of star-forming galaxies, and the chemical enrichment, dust attenuation, and photoionization conditions. As the stellar metallicity decreases toward high redshift (e.g., Cullen et al. 2019; Kashino et al. 2022), the ionizing efficiency of stellar populations increases (see also Figure 14) yielding higher line luminosities at fixed SFR in general. Further, the harder spectra of these stellar populations lead to higher excitation conditions (e.g., Steidel et al. 2016) that primarily result in an increasing [O III] luminosity as long as the gas-phase metallicity is above  $12 + \log(O/H) \gtrsim 7.5$  (Figure 15). Finally, most star formation in galaxies in the  $z \approx 2$  universe occurs in objects with a relatively high mass  $\sim 10^{10} M_{\odot}$  (e.g., Davidzon et al. 2017; Chruslinska & Nelemans 2019; Behroozi et al. 2019), which have significantly higher metallicity (Sanders et al. 2021), dust attenuation (Garn & Best 2010), and lower ionizing photon production efficiency (e.g., Atek et al. 2022). Therefore, while the rate at which galaxies form stars is lower at higher redshifts, the lower metallicities of the stellar atmospheres and interstellar media make these galaxies in comparison much more luminous in [O III] (see also Figure 8). In this picture, it is indeed not a surprise that we measure a typical [O III]/ $H\beta$  that is close to the maximum expected in star-forming galaxies ([O III] $_{5008}/H\beta \approx 7$ ; e.g., Bian et al. 2018).

At some point, these favorable conditions for [O III] emission should no longer be balanced by the declining SFR density. Further, the [O III] luminosity decreases at even lower metallicities than the ones that characterize our sample (as indicated by our stacking results in Figure 17). These processes combined should lead to a rapid decline in  $\rho_{[\text{O III}]}$  at  $z > 6$  that could potentially be probed by future JWST observations in redder NIRCcam filters. Likewise, it is plausible that the [O III] luminosity declines rapidly in a significant fraction of galaxies with masses below  $< 10^7 M_{\odot}$ , which would lead to a flattening of the [O III] LF toward fainter luminosities, and a less dramatic difference between the evolution





**Figure 17.** The relation between gas-phase metallicity and stellar mass at  $z \sim 6$  for galaxies and stacks with direct  $T_e$ -based or strong-line-based metallicity estimates. The horizontal errors show the boundaries of the subsets (pentagons) and the 16th–84th percentiles of masses in the full stack (star), respectively. The solar metallicity (Asplund et al. 2009) is highlighted in orange. We highlight the systematic uncertainty between different strong-line calibrations in the bottom right. We find that recent measurements in individual galaxies (Curti et al. 2023) roughly scatter around the metallicity of our median stack of  $z \sim 6.5$  [O III] emitters. The average metallicity is slightly higher than expectations from the FIRE simulation (Ma et al. 2016), once these have been rescaled to match the mass–metallicity relation at  $z \approx 3$  (Sanders et al. 2021).

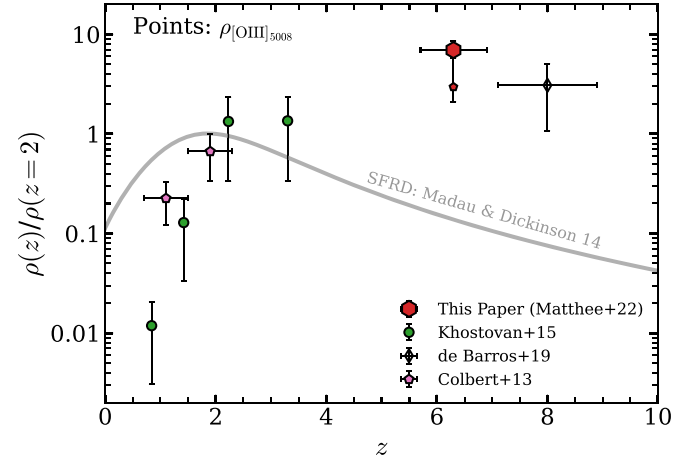


**Figure 18.** The field UV luminosity function of our sample of [O III] emitters at  $z = 5.33$ – $6.96$ , masking the redshift around the quasar (hexagons). Open hexagons show the number densities without correcting for completeness and the maximum volume of each individual source. The number densities match the UV luminosity function of UV-selected galaxies at  $z \sim 6$  by Bouwens et al. (2021) at  $-21.0 < M_{UV} < -19.5$ . This demonstrates that the strong lines are typical for most  $z \sim 6$  galaxies. At fainter UV luminosities, our line-selected sample only picks up the upper end of the EW distribution. Cosmic variance is likely important at the bright end.

of  $\rho_{[\text{O III}]}$  and the SFR density once we would integrate to fainter luminosity limits. Characterizing such flattening of the [O III] LF should be performed with deeper complete emission-line surveys.

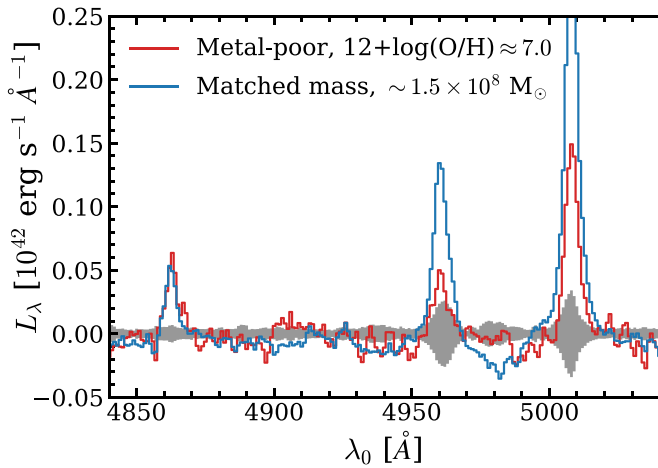
## 6.2. The Role of Galaxies during Reionization

A prime goal of our EIGER survey is to observe the role of galaxies in the reionization of the universe, in particular using



**Figure 19.** The field [O III]<sub>5008</sub> luminosity density (integrated down to a limiting luminosity of  $10^{42.2}$  erg  $s^{-1}$ ) as a function of redshift, scaled to the density at  $z = 2$ . Our results based on JWST spectroscopy are shown as a red hexagon (assuming a faint-end slope  $\alpha = -2$ , see Section 4.3). The small red pentagon shows our results for our fit with varying faint-end slope (best-fit  $\alpha = -0.2$ ), showing that this does not significantly affect our results. The SED-inferred [O III] luminosity density at  $z \sim 8$  is shown as open diamond (De Barros et al. 2019). Green circles show the narrow-band luminosity densities measured by Khostovan et al. (2015), and the pink data points show results from the HST grisms at lower redshifts (Colbert et al. 2013). The gray line shows the evolution of the cosmic star formation rate density from Madau & Dickinson (2014), also scaled to  $z = 2$ .

the cross-correlation between galaxies and Ly $\alpha$  forest data in the quasar spectra. The ability to simultaneously measure the ionizing emissivity  $\xi_{\text{ion}}$  for these galaxies is promising. Generally, our measured  $\log_{10}(\xi_{\text{ion}}/\text{Hz erg}^{-1}) = 25.31^{+0.29}_{-0.16}$  is somewhat higher than the canonical values that have been assumed when modeling the role of galaxies in the reionization



**Figure 20.** The stacked spectrum of the five metal-poor low mass galaxies with the lowest  $[\text{O III}]/\text{H}\beta$  ratios (where  $\text{H}\beta$  was detected with  $S/N > 5$ ; red) of galaxies compared to the stacked spectrum of galaxies with comparable mass (blue).

of the universe (e.g., Robertson et al. 2013). The high values of  $\xi_{\text{ion}}$  imply that more modest values of the escape fraction of ionizing photons are needed for galaxies to reionize the universe by  $z \approx 6$  (e.g., Davies et al. 2021), or that the contribution from very faint galaxies is minor ( $M_{\text{UV}} > -17$ , e.g., Matthee et al. 2022b).

As shown in Paper I, we find clear indications of an excess  $\text{Ly}\alpha$  and  $\text{Ly}\beta$  transmission at a distance of  $\approx 5$  cMpc around  $[\text{O III}]$  emitters at  $z \approx 6$  in this single quasar sight line. This demonstrates the local enhancement in the ionizing emissivity around galaxies and supports an important role of galaxies in the end stages of cosmic reionization. With the full EIGER data, our simultaneous measurement of  $\xi_{\text{ion}}$  may enable us to constrain the escape fraction and contribution of faint unseen galaxies using a larger sample of quasar sight lines (e.g., Kakiichi et al. 2018; Meyer et al. 2020).

### 6.3. The Most Metal-poor Galaxies in Our Sample

The early results on the gas-phase metallicities in  $z \sim 6-7$  galaxies (Section 5.3) suggest that there are significant metallicity variations. As can be seen in Figure 15, the five objects with the lowest  $[\text{O III}]/\text{H}\beta$  ratios ( $\lesssim 3$ ) appear among the intermediate masses probed by our sample. We show the stacked spectrum of these five galaxies in Figure 20, where we compare it to the stacked spectrum of all galaxies with similar mass. We need to rely on strong-line calibrations to estimate the gas-phase metallicities of these galaxies, which are particularly uncertain at these  $[\text{O III}]/\text{H}\beta$  ratios if one assumes that they are on the lower metallicity branch (see, e.g., Curti et al. 2023). Using the two calibrations that encapsulate the range of possible values (Bian et al. 2018; Nakajima et al. 2022), we find a metallicity in the range  $12+\log(\text{O}/\text{H}) = (6.8-7. \pm 0.1)$  (i.e., 1%–2% solar). These metallicities are  $\approx 0.6$  dex lower than the metallicity estimated for the comparison sample (Table 3), confirming the significant scatter in metallicities at fixed mass. A more detailed investigation of the properties of these systems requires further spectroscopic follow-up observations that can verify the metallicities and characterize the full SED. The fact that these objects can be identified in NIRCcam WFSS data is promising for statistical studies of the properties of low metallicity galaxies.

### 6.4. On the Efficiency of NIRCcam WFSS Surveys

Finally, with the aim of the community planning future JWST observations, we reflect on the efficiency and challenges of NIRCcam WFSS surveys based on our first analyses.

The main limitation in WFSS is the spectral contamination and the association between spectral features and galaxies. The latter is particularly challenging in the case of a single line detection with high equivalent width where the continuum trace is not visible. Typically, both issues are mitigated by observing the field with multiple (ideally orthogonal) dispersion directions (e.g., Brammer et al. 2012). However, obtaining multiple orthogonal dispersion directions with NIRCcam is relatively inefficient. Nevertheless, we find that several factors significantly mitigate these issues, specifically when searching for emission-line doublets. These are the high spectral resolution ( $R \sim 1500$ ) and the relatively flat continuum spectrum of the main foreground population at  $3.5 \mu\text{m}$  such that continuum contamination can be cleaned out very efficiently thanks to the high contrast of narrow emission lines (see Figure 1). The use of doublets (or sets of relatively nearby lines as  $\text{H}\beta + [\text{O III}]$ ) further allows a precise estimate of the observed wavelength of the lines. This facilitates the galaxy–line association significantly, even in the 80% of our survey area that is only observed with a single-dispersion direction. For galaxies with single lines (such as  $\text{H}\alpha$  emitters in practice are), the correct line–galaxy association in single-dispersion WFSS data requires either morphological information and/or prior constraints on the redshift from broadband colors.

Generally, the main strengths of a NIRCcam/WFSS survey are spectra for a complete coverage of all objects within the field of view without photometric preselection, the ability to perform spatially resolved studies, and robustness against uncertainties in slit-losses or uncontrolled contamination (e.g., Maseda et al. 2019). Indeed, our survey has efficiently yielded redshifts for  $>100$   $[\text{O III}]$  emitters at  $z = 5.3-7$  already in 18.5 hr of JWST observing time including overheads. A similar number of  $\text{H}\alpha$  emitters at  $z = 3-5$  (to be explored in future analyses), and several spatially resolved lower redshift  $z \approx 1-3$  lines from the Paschen and Brackett series, and infrared lines as He I and Fe II (e.g., Brinchmann 2022) are further lurking in the data. Additionally, thanks to the design of NIRCcam, JWST can simultaneously obtain very sensitive  $<2.4 \mu\text{m}$  imaging in the same field of view. All things combined, we conclude that, thanks to the brightness of the  $[\text{O III}]$  doublet in high-redshift galaxies, NIRCcam WFSS surveys will be particularly efficient in mapping the complete distribution of star-forming galaxies with  $M_{\text{star}} \gtrsim 10^7 M_{\odot}$  from  $z \approx 3$  to 9 in the field of view.

## 7. Summary

It is a key aim to characterize the physical conditions of high-redshift galaxies in order to understand early galaxy formation and probe the Epoch of Reionization. Here, we use the first deep  $3.5 \mu\text{m}$  WFSS JWST observations of the EIGER program to analyze the properties of 117 spectroscopically confirmed  $[\text{O III}]$  emitters at  $z = 5.33-6.93$  in the field of the luminous quasar J0100+2802. The F356W WFSS observations are complemented with NIRCcam imaging in the F115W, F200W, and F356W filters. These first deep observations demonstrate the excellent performance of WFSS using JWST/NIRCcam in identifying large

complete samples of distant galaxies (see Paper I). Our main results are summarized in the following points:

1. Using an automated search algorithm that detects [O III]<sub>4960,5008</sub> and [O III]+H $\beta$  pairs with S/N  $\geq 3$  in the grism data, we identify a total of 133 resolved [O III] emitting components, of which 68 show additional H $\gamma$  detections and 2 show H $\gamma$ .
2. We find that a large number of [O III] emitters are closely separated, with a strong excess clustering at  $< 2''$ . All such close pairs are physically associated ( $|\Delta z| \lesssim 600 \text{ km s}^{-1}$ ). In order not to have our sample selection depend on the spatial resolution, deblending parameters and our orientation to the objects, we merge all closely separated pairs in so-called systems and treat them as one of the 117 galaxies that constitute our sample.
3. By self-consistently modeling the nebular and stellar components that contribute to the observed SEDs and fitting this to the spectral and photometric data, we find that the galaxies in our sample are characterized by relatively young ages ( $\approx 100 \text{ Myr}$ ) and low dust attenuation ( $E(B - V) \approx 0.1$ ). Our sample spans a wide UV luminosity range  $M_{\text{UV}} = -17.7 - M_{\text{UV}} = -22.3$ , and the masses are typically small ( $\approx 2 \times 10^8 M_{\odot}$ ), while in total spanning 3 orders of magnitude ( $10^{6.8-10.1} M_{\odot}$ ).
4. We spectroscopically measure an average H $\beta$ + [O III] EW of  $948_{-138}^{+192} \text{ \AA}$  for UV bright galaxies ( $M_{\text{UV}} < -20.5$ ). This confirms that such extreme rest-frame optical EWs that are very rare in the local universe ( $< 1\%$  of SDSS) are typical in the Epoch of Reionization. Our SED models suggest a typical increasing EW with decreasing stellar mass, increasing from an EW  $\approx 850 \text{ \AA}$ , at the typical UV luminosity of  $M_{\text{UV}} \approx -19.6$ , up to EWs  $\approx 3000 \text{ \AA}$  for our most extreme systems with masses  $M_{\text{star}} \sim 10^7 M_{\odot}$ .
5. We present the [O III] luminosity function (LF) in the field (i.e., masking the quasar environment) at  $z \sim 6$ , the first spectroscopic measurement at  $z > 1.5$ . The luminosity function is slightly higher compared to measurements at  $z \approx 3$  and comparable to recent inferences at  $z \sim 8$  based on SED modeling. The UV LF of [O III] emitters matches the UV LF of LBGs at  $z \sim 6$  relatively well, except for the bright and faint ends. This demonstrates that, in general, strong [O III] emission is typical among LBGs. While the bright end is likely subject to significant cosmic variance, our lower number density for the UV faintest luminosities shows that we are only picking up the extreme tail of the EW distribution for those objects.
6. The sensitive spectroscopy allows us to explore the physical conditions in our sample of  $z \sim 6$  galaxies using detections of [O III]<sub>4364</sub> in stacks and H $\gamma$ , H $\beta$ , and [O III]<sub>4960,5008</sub> in stacks and individual sources. We measure  $\xi_{\text{ion}}$ , the ionizing photon production efficiency of galaxies, to be  $10^{25.31_{-0.16}^{+0.29}} \text{ Hz erg}^{-1}$ , which is slightly higher than that typically assumed in calculations of the reionization budget of star-forming galaxies. The galaxies are further characterized by little nebular dust attenuation  $E(B - V) = 0.14_{-0.14}^{+0.16}$ , and an SFR  $\approx 5 M_{\odot} \text{ yr}^{-1}$ .
7. Typically, our sample is characterized by a very high [O III]/H $\beta$  ratio, which suggests that the ISM in the average galaxy in our sample has a high ionization parameter and a gas-phase metallicity that optimizes the [O III]/H $\beta$  ratio. The [O III]/H $\beta$  ratio varies nonmonotonically with mass, peaking at  $\sim 10^8 M_{\odot}$  and declining

slightly to both higher and lower masses. This behavior can be explained in the context of an MZR and the double-valued behavior of [O III]/H $\beta$  and metallicity.

8. Our detection of [O III]<sub>4364</sub> yields an average metallicity  $12 + \log(\text{O}/\text{H}) = 7.38 \pm 0.09$  and supports the use of strong-line calibrations to derive the MZR at  $z \sim 6$ , which have a slope and evolution compared to  $z \sim 3$  roughly matching expectations from hydrodynamical simulations. We further detect several intermediate mass galaxies with relatively low [O III]/H $\beta$  suggesting that they are very metal-poor, 1%–2% solar, and demonstrating significant scatter at fixed mass.
9. We show that the strong [O III] EWs in high-redshift galaxies lead to an [O III] luminosity density that is a factor  $\approx 2$ –5 higher at  $z \sim 6$  compared to the peak of the cosmic SFR density at  $z \sim 2$ , despite the order of magnitude decline in cosmic SFR. As discussed in Section 6.1, we argue that this is due to a complex combination of an SFR that is increasingly dominated by lower mass galaxies toward higher redshifts. These galaxies have a higher production efficiencies of ionizing photons, lower gas-phase metallicity, and lower dust attenuation compared to the more massive galaxies that dominate the SFR density at  $z \approx 2$ . All these factors combined enhance the emerging [O III] luminosity at  $z \approx 6$ , compared to  $z \approx 2$ .

The main implication of this paper for future observations is that the abundant strong [O III] emission lines from galaxies in the early universe, combined with the ease with which continuum contamination can be removed, make NIRC*am* WFSS observations a highly efficient mode to spectroscopically map the galaxy distribution from the peak of star formation to the Epoch of Reionization. Main open questions are whether and when the faint-end slope of the [O III] luminosity function flattens compared to the galaxy SFR function due to the increasingly lower metallicities at lower masses. The unanticipated sensitivity to detect fainter lines as H $\gamma$  and [O III]<sub>4364</sub> is promising for the study of dust attenuation, star formation, gas-phase metallicity, and the ionizing production efficiency of galaxies. The complete samples selected from the WFSS data will further allow clustering measurements and spatially resolved properties (colors, line ratios) from the emission-line galaxies, which we will explore in future work. Simultaneous measurements of ionizing production efficiency and the Ly $\alpha$  forest transmission in the full EIGER sample may offer promising perspectives on the contributions of various galaxy populations to cosmic reionization.

We thank an anonymous referee for a constructive report. We thank Norbert Pirzkal for advice on spectral extraction methods, the JAGUAR and *Mirage* teams (Williams et al. 2018; Hilbert et al. 2019) for making extremely useful data sets and software available to help developing our reduction and analysis pipelines, and Rohan Naidu for useful comments on SED fitting.

This work is based on observations made with the NASA/ESA/CSA James Webb Space Telescope. The data were obtained from the Mikulski Archive for Space Telescopes at the Space Telescope Science Institute, which is operated by the Association of Universities for Research in Astronomy, Inc.,

under NASA contract NAS 5–03127 for JWST. These observations are associated with program # 1243.

All of the data presented in this paper were obtained from the Mikulski Archive for Space Telescopes (MAST) at the Space Telescope Science Institute. The specific observations analyzed can be accessed via <https://doi.org/10.17909/yc3h-jn44>.

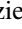



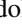
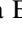
This research made use of the open-source Python package *Mirage*, the JWST Multi Instrument Ramp Generator (Hilbert et al. 2019). This research made use of *Photutils*, an *Astropy* package for detection and photometry of astronomical sources (Bradley et al. 2022).

This work has been supported by JSPS KAKENHI grant No. JP21K13956 (D.K.). R.S. acknowledges support from NASA award No. HST-GO-15085.001.

*Facility:* JWST.

*Software:* Python, *matplotlib* (Hunter 2007), *numpy* (Oliphant 2015), *scipy* (Virtanen et al. 2020), *Astropy* (Astropy Collaboration et al. 2013, 2018).

## ORCID iDs

Jorryt Matthee  <https://orcid.org/0000-0003-2871-127X>  
 Ruari Mackenzie  <https://orcid.org/0000-0003-0417-385X>  
 Robert A. Simcoe  <https://orcid.org/0000-0003-3769-9559>  
 Daichi Kashino  <https://orcid.org/0000-0001-9044-1747>  
 Simon J. Lilly  <https://orcid.org/0000-0002-6423-3597>  
 Rongmon Bordoloi  <https://orcid.org/0000-0002-3120-7173>  
 Anna-Christina Eilers  <https://orcid.org/0000-0003-2895-6218>

## References

- Alam, S., Albareti, F. D., Allende Prieto, C., et al. 2015, *ApJS*, 219, 12
- Asplund, M., Grevesse, N., Sauval, A. J., & Scott, P. 2009, *ARA&A*, 47, 481
- Astropy Collaboration, Price-Whelan, A. M., Sipőcz, B. M., et al. 2018, *AJ*, 156, 123
- Astropy Collaboration, Robitaille, T. P., Tollerud, E. J., et al. 2013, *A&A*, 558, A33
- Atek, H., Furtak, L. J., Oesch, P., et al. 2022, *MNRAS*, 511, 4464
- Behroozi, P., Wechsler, R. H., Hearin, A. P., & Conroy, C. 2019, *MNRAS*, 488, 3143
- Bertin, E., & Arnouts, S. 1996, *A&AS*, 117, 393
- Bian, F., Kewley, L. J., & Dopita, M. A. 2018, *ApJ*, 859, 175
- Bouwens, R. J., Illingworth, G. D., Oesch, P. A., et al. 2014, *ApJ*, 793, 115
- Bouwens, R. J., Oesch, P. A., Stefanon, M., et al. 2021, *AJ*, 162, 47
- Bouwens, R. J., Smit, R., Labbé, I., et al. 2016, *ApJ*, 831, 176
- Boyer, M. L., Anderson, J., Gennaro, M., et al. 2022, *RNAAS*, 6, 191
- Boyle, K. N. K., Stark, D. P., Bunker, A. J., Tang, M., & Maseda, M. V. 2022, *MNRAS*, 513, 4451
- Bradley, L., Sipőcz, B., Robitaille, T., et al. 2022, *astropy/photutils*: 1.5.0, Zenodo, doi:10.5281/zenodo.6825092
- Brammer, G. B., van Dokkum, P. G., Franx, M., et al. 2012, *ApJS*, 200, 13
- Brinchmann, J. 2022, arXiv:2208.07467
- Brinchmann, J., Inami, H., Bacon, R., et al. 2017, *A&A*, 608, A3
- Bunker, A., Wilkins, S., Ellis, R., et al. 2010, *MNRAS*, 409, 855
- Bunker, A. J. & NIRSPEC Instrument Science Team/JAES Collaboration 2020, in IAU Symp. 352, *Uncovering Early Galaxy Evolution in the ALMA and JWST Era*, ed. E. da Cunha et al. (Cambridge: Cambridge Univ. Press), 342
- Byler, N., Dalcanton, J. J., Conroy, C., & Johnson, B. D. 2017, *ApJ*, 840, 44
- Calzetti, D., Armus, L., Bohlin, R. C., et al. 2000, *ApJ*, 533, 682
- Cardelli, J. A., Clayton, G. C., & Mathis, J. S. 1989, *ApJ*, 345, 245
- Carnall, A. C., Begley, R., McLeod, D. J., et al. 2023, *MNRAS Lett.*, 518, L45
- Chabrier, G. 2003, *PASP*, 115, 763
- Chen, Z., Stark, D. P., Endsley, R., et al. 2023, *MNRAS*, 518, 5607
- Choi, J., Dotter, A., Conroy, C., et al. 2016, *ApJ*, 823, 102
- Chruslinska, M., & Nelemans, G. 2019, *MNRAS*, 488, 5300
- Colbert, J. W., Teplitz, H., Atek, H., et al. 2013, *ApJ*, 779, 34
- Cullen, F., McLure, R. J., Dunlop, J. S., et al. 2019, *MNRAS*, 487, 2038
- Curti, M., D'Eugenio, F., Carniani, S., et al. 2023, *MNRAS*, 518, 425
- Davidzon, I., Ilbert, O., Laigle, C., et al. 2017, *A&A*, 605, A70
- Davies, F. B., Bosman, S. E. I., Furlanetto, S. R., Becker, G. D., & D'Aloisio, A. 2021, *ApJL*, 918, L35
- De Barros, S., Oesch, P. A., Labbé, I., et al. 2019, *MNRAS*, 489, 2355
- Dotter, A. 2016, *ApJS*, 222, 8
- Duncan, K., & Conselice, C. J. 2015, *MNRAS*, 451, 2030
- Einasto, J., Klypin, A. A., Saar, E., & Shandarin, S. F. 1984, *MNRAS*, 206, 529
- Endsley, R., Stark, D. P., Chevallard, J., & Charlot, S. 2021, *MNRAS*, 500, 5229
- Endsley, R., Stark, D. P., Whitler, L., et al. 2022, arXiv:2208.14999
- Ferland, G. J., Korista, K. T., Verner, D. A., et al. 1998, *PASP*, 110, 761
- Finkelstein, S. L. 2016, *PASA*, 33, e037
- Finkelstein, S. L., Bagley, M., Song, M., et al. 2022, *ApJ*, 928, 52
- Gaia Collaboration, Brown, A. G. A., Vallenari, A., et al. 2018, *A&A*, 616, A1
- Garn, T., & Best, P. N. 2010, *MNRAS*, 409, 421
- Gelli, V., Salvadori, S., Ferrara, A., Pallottini, A., & Carniani, S. 2021, *ApJL*, 913, L25
- Harikane, Y., Ouchi, M., Inoue, A. K., et al. 2020, *ApJ*, 896, 93
- Hashimoto, T., Inoue, A. K., Mawatari, K., et al. 2019, *PASJ*, 71, 71
- Hilbert, B., Sahlmann, J., Volk, K., et al. 2019, *spacetelescope/mirage*: First github release, v1.1.1, Zenodo, doi:10.5281/zenodo.3519262
- Hunter, J. D. 2007, *CSE*, 9, 90
- Inoue, A. K., Tamura, Y., Matsuo, H., et al. 2016, *Sci*, 352, 1559
- Izotov, Y. I., Guseva, N. G., Fricke, K. J., et al. 2021a, *A&A*, 646, A138
- Izotov, Y. I., Worseck, G., Schaerer, D., et al. 2021b, *MNRAS*, 503, 1734
- Izotov, Y. I., Worseck, G., Schaerer, D., et al. 2018, *MNRAS*, 478, 4851
- Johnson, B. D., Leja, J., Conroy, C., & Speagle, J. S. 2021, *ApJS*, 254, 22
- Janeau, S., Dickinson, M., Alexander, D. M., & Salim, S. 2011, *ApJ*, 736, 104
- Kakiichi, K., Ellis, R. S., Laporte, N., et al. 2018, *MNRAS*, 479, 43
- Kashino, D., Lilly, S. J., Matthee, J., et al. 2023, *ApJ*, 950, 66
- Kashino, D., Lilly, S. J., Renzini, A., et al. 2022, *ApJ*, 925, 82
- Katz, H., Saxena, A., Cameron, A. J., et al. 2023, *MNRAS*, 518, 592
- Kennicutt, R. C., & Evans, N. J. 2012, *ARA&A*, 50, 531
- Khostovan, A. A., Sobral, D., Mobasher, B., et al. 2015, *MNRAS*, 452, 3948
- Khostovan, A. A., Sobral, D., Mobasher, B., et al. 2016, *MNRAS*, 463, 2363
- Kusakabe, H., Blaizot, J., Garel, T., et al. 2020, *A&A*, 638, A12
- Labbé, I., Oesch, P. A., Bouwens, R. J., et al. 2013, *ApJL*, 777, L19
- Leitherer, C., Schaerer, D., Goldader, J., et al. 1999, *ApJS*, 123, 3
- Luridiana, V., Morisset, C., & Shaw, R. A. 2015, *A&A*, 573, A42
- Ma, X., Hopkins, P. F., Kasen, D., et al. 2016, *MNRAS*, 459, 3614
- Madau, P. 1995, *ApJ*, 441, 18
- Madau, P., & Dickinson, M. 2014, *ARA&A*, 52, A15
- Malkan, M. A., Cohen, D. P., Maruyama, M., et al. 2017, *ApJ*, 850, 5
- Mármol-Queraltó, E., McLure, R. J., Cullen, F., et al. 2016, *MNRAS*, 460, 3587
- Maseda, M. V., Franx, M., Chevallard, J., & Curtis-Lake, E. 2019, *MNRAS*, 486, 3290
- Matthee, J., Feltre, A., Maseda, M., et al. 2022a, *A&A*, 660, A10
- Matthee, J., Naidu, R. P., Pezzulli, G., et al. 2022b, *MNRAS*, 512, 5960
- Matthee, J., Sobral, D., Best, P., et al. 2017, *MNRAS*, 465, 3637
- Matthee, J., Sobral, D., Hayes, M., et al. 2021, *MNRAS*, 505, 1382
- Merlin, E., Bonchi, A., Paris, D., et al. 2022, *ApJL*, 938, L14
- Meyer, R. A., Kakiichi, K., Bosman, S. E. I., et al. 2020, *MNRAS*, 494, 1560
- Micheva, G., Oey, M. S., Jaskot, A. E., & James, B. L. 2017, *ApJ*, 845, 165
- Moustakas, J., & Kennicutt, R. C. J. 2006, *ApJS*, 164, 81
- Naidu, R. P., Matthee, J., Oesch, P. A., et al. 2022, *MNRAS*, 510, 4582
- Nakajima, K., Ouchi, M., Xu, Y., et al. 2022, *ApJS*, 262, 3
- Oliphant, T. E. 2015, *Guide to NumPy* (Austin, TX: Continuum Press)
- Pilyugin, L. S., Thuan, T. X., & Vilchez, J. M. 2006, *MNRAS*, 367, 1139
- Planck Collaboration, Aghanim, N., Akrami, Y., et al. 2020, *A&A*, 641, A6
- Raiter, A., Fosbury, R. A. E., & Teimoorinia, H. 2010, *A&A*, 510, A109
- Reddy, N. A., Oesch, P. A., Bouwens, R. J., et al. 2018a, *ApJ*, 853, 56
- Reddy, N. A., Shapley, A. E., Sanders, R. L., et al. 2018b, *ApJ*, 869, 92
- Reddy, N. A., Steidel, C. C., Pettini, M., & Bogosavljević, M. 2016, *ApJ*, 828, 107
- Reines, A. E., Nidever, D. L., Whelan, D. G., & Johnson, K. E. 2010, *ApJ*, 708, 26
- Rhoads, J. E., Wold, I. G. B., Harish, S., et al. 2023, *ApJL*, 942, L14
- Rieke, M. J., Kelly, D. M., Misselt, K., et al. 2023, *PASP*, 135, 028001
- Rigby, J., Perrin, M., McElwain, M., et al. 2023, *PASP*, 135, 048001
- Roberts-Borsani, G. W., Bouwens, R. J., Oesch, P. A., et al. 2016, *ApJ*, 823, 143
- Robertson, B. E., Furlanetto, S. R., Schneider, E., et al. 2013, *ApJ*, 768, 71
- Sanders, R. L., Shapley, A. E., Jones, T., et al. 2021, *ApJ*, 914, 19
- Sanders, R. L., Shapley, A. E., Kriek, M., et al. 2016, *ApJ*, 816, 23
- Sanders, R. L., Shapley, A. E., Reddy, N. A., et al. 2020, *MNRAS*, 491, 1427

- Schaerer, D. 2003, *A&A*, 397, 527
- Schaerer, D., & de Barros, S. 2009, *A&A*, 502, 423
- Schaerer, D., Izotov, Y. I., Verhamme, A., et al. 2016, *A&A*, 591, L8
- Schaerer, D., Marques-Chaves, R., Barrufet, L., et al. 2022, *A&A*, 665, L4
- Schechter, P. 1976, *ApJ*, 203, 297
- Schlawin, E., Leisenring, J., Misselt, K., et al. 2020, *AJ*, 160, 231
- Schmidt, M. 1968, *ApJ*, 151, 393
- Shibuya, T., Ouchi, M., & Harikane, Y. 2015, *ApJS*, 219, 15
- Shivaei, I., Reddy, N. A., Siana, B., et al. 2018, *ApJ*, 855, 42
- Smit, R., Bouwens, R. J., Labbé, I., et al. 2014, *ApJ*, 784, 58
- Sobral, D., Santos, S., Matthee, J., et al. 2018, *MNRAS*, 476, 4725
- Springel, V., White, S. D. M., Tormen, G., & Kauffmann, G. 2001, *MNRAS*, 328, 726
- Stark, D. P., Ellis, R. S., & Ouchi, M. 2011, *ApJL*, 728, L2
- Stark, D. P., Schenker, M. A., Ellis, R., et al. 2013, *ApJ*, 763, 129
- Steidel, C. C., Giavalisco, M., Pettini, M., Dickinson, M., & Adelberger, K. L. 1996, *ApJL*, 462, L17
- Steidel, C. C., Strom, A. L., Pettini, M., et al. 2016, *ApJ*, 826, 159
- Sun, F., Egami, E., Pirzkal, N., et al. 2022a, *ApJL*, 936, L8
- Sun, F., Egami, E., Pirzkal, N., et al. 2022b, arXiv:2209.03374
- Tacchella, S., Johnson, B. D., Robertson, B. E., et al. 2022, arXiv:2208.03281
- Tamura, Y., Mawatari, K., Hashimoto, T., et al. 2019, *ApJ*, 874, 27
- Tang, M., Stark, D. P., Chevallard, J., & Charlot, S. 2019, *MNRAS*, 489, 2572
- Tang, M., Stark, D. P., Ellis, R. S., et al. 2022, *MNRAS*, 509, 3102
- Taylor, A. J., Barger, A. J., & Cowie, L. L. 2022, *ApJL*, 939, L3
- Theios, R. L., Steidel, C. C., Strom, A. L., et al. 2019, *ApJ*, 871, 128
- Topping, M. W., Stark, D. P., Endsley, R., et al. 2022, *ApJ*, 941, 153
- Trump, J. R., Arrabal Haro, P., Simons, R. C., et al. 2023, *ApJ*, 945, 35
- van der Wel, A., Straughn, A. N., Rix, H.-W., et al. 2011, *ApJ*, 742, 111
- Virtanen, P., Gommers, R., Oliphant, T. E., et al. 2020, *NatMe*, 17, 261
- Wang, R., Wu, X.-B., Neri, R., et al. 2016, *ApJ*, 830, 53
- Williams, C. C., Curtis-Lake, E., Hainline, K. N., et al. 2018, *ApJS*, 236, 33
- Witstok, J., Smit, R., Maiolino, R., et al. 2022, *MNRAS*, 515, 1751
- Wu, X.-B., Wang, F., Fan, X., et al. 2015, *Natur*, 518, 512
- Yang, H., Malhotra, S., Gronke, M., et al. 2017, *ApJ*, 844, 171
- Zackrisson, E., Bergvall, N., & Leitert, E. 2008, *ApJL*, 676, L9